Theoretical Study on Electric Field Control of Magnetism in 2D Materials

Nguyen Thi Phuong Thao

Graduate School of Engineering
Osaka University

This dissertation is submitted for the degree of
Doctor of Philosophy

December 2020

I would like to dedicate this thesis to my loving parents.

Declaration

I hereby declare that except where specific reference is made to the work of others, the contents of this dissertation are original and have not been submitted in whole or in part for consideration for any other degree or qualification in this, or any other university. This dissertation is my own work and contains nothing which is the outcome of work done in collaboration with others, except as specified in the text and Acknowledgements.

Nguyen Thi Phuong Thao
December 2020

Acknowledgements

First of all, I would like to express my deep gratitude to Prof. Tamio Oguchi for his conscientious supervision and encouragements in my study, for his patience, motivation, and immense knowledge. I also wish to express my special thanks to Dr. Kunihiko Yamauchi, who is my enthusiastic mentor and also friend during my Ph.D study.

I sincerely acknowledge Prof. Yoshitada Morikawa, Prof. Satoshi Hamaguchi and Prof. Kazunori Sato for their helpful comments and criticisms for my Ph.D thesis. I also acknowledge valuable discussions from Prof. Kohji Nakamura, Prof. Silvia Piccozzi and Dr. Danila Amoroso and helpful suggestions and advice from other staffs of Oguchi laboratory; Prof. Koun Shirai, Dr. Hiroyoshi Momida, Dr. Testuya Fukushima, Dr. Tomoki Yamashita. I wish to give many thanks to our secretaries Mrs. Mika Asada and Ms. Chiaki Kurabayashi for their kind assistance.

Finally, I wish to thank my parents and my fiancée for their warmhearted support.

Abstract

The electric field control of magnetism and magnetic properties has been achieved across several different materials systems in the fields of information storage and processing. For example, applying an electric field to ferromagnetic metals changes the Fermi level position at the interface that governs the magnetocrystalline anisotropy of the metal systems. In two-dimensional (2D) materials, voltage-controlled switching between antiferromagnetic and ferromagnetic states has been reported as a promising feature for potential applications.

This thesis presents the first-principles study based on the density functional theory in the effect of the electric field in such materials, discusses our current understanding of the mechanisms. Firstly, the magnetocrystalline anisotropy of Co-based 3*d* transition-metal thin films is systematically investigated. The computational results predict that large perpendicular magnetocrystalline anisotropy can be achieved by tuning the atomic-layer alignments in Ni-Co thin film. I discovered that not only the on-site spin-orbit coupling of 3*d* elements determines the magnetocrystalline anisotropy energy but also the strong hybridization between these elements plays a constructive role to enhance the perpendicular magnetocrystalline anisotropy. The effect of the external electric field in the magnetocrystalline anisotropy is small in this Co-based thin film due to large screening effect in metallic system. Thus, playing with an insulating material to reduce the charge screening effect can promote the application of electric field.

Following by the above study, I focus on the electric field effect on magnetic properties of 2D VI_3 bilayer. My first-principles analysis highlights the role of trigonal crystal-field effects in comparison with the CrI_3 prototypical case, where the effects are absent. In VI_3 bilayers, the empty a_{1g} state - consistent with the observed trigonal distortion - is found to play a crucial role in both stabilizing the insulating state and in determining the inter-layer magnetic interaction in two different VI_3 stackings (labelled AB and AB'). Upon application of electric fields perpendicular to the slab, I find that the magnetic ground-state in the AB' stacking can be switched from antiferromagnetic to ferromagnetic, suggesting VI_3 bilayer as an appealing candidate for electric-field-driven miniaturized spintronic devices.

Table of contents

List of figures

List of tables

Nomenclature

Greek Symbols

e	Electron
$\hbar$	Reduced Planck constant

Acronyms / Abbreviations

AFM	Aniferromagnetic
CEF	Crystalline Electric Field
DFT	Density Functional Theory
FM	Ferromagnetic
GGA	Generalized Gradient Approximation
MAE	Magnetocrystalline Anisotropy Energy
MA	Magnetocrystalline Anisotropy
MLWFs	Maximally Localized Wannier Functions
MRAM	Magnetic Random Access Memory
PMA	Perpendicular Magnetocrystalline Anisotropy
SOC	Spin-orbit Coupling
WFs	Wannier Functions

Chapter 1

Introduction

The idea of using electric fields to control magnetism dates back to the 1960s has received much attention recently on spintronics applications [1, 2]. Using applied-voltage to control magnetism is increasingly used to realize magnetic random access memories and standby-power-free integrated circuits that rely on non-volatile information encoded in the direction of magnetization [3, 4]. The electric-field manipulation of magnetism is of interest not only because of its technological importance but also because it allows us to uncover properties of magnetic materials that are otherwise inaccessible. This thesis focuses on the current state of the electric-field manipulation of magnetism in different magnetic materials. The effect of the electric field, such as applying an electric field to a thin film to control the magnetization direction through the magnetic anisotropy, and control the magnetic stability of the 2D magnetic bilayer system, are covered elsewhere. This thesis is organized as follows.

Chapter 2 introduces the theoretical backgrounds for this thesis. A density functional theory is widely used in condensed matter physics to calculate the band structure of solids and electronic properties. In calculating the electronic structure of strongly correlated electron systems, considering the relativistic effect is also important, especially to treat with the spin-orbit coupling. A strongly correlated electron system with a classical spin model and the Hubbard model is introduced.

In Chapter 3, the magnetocrystalline anisotropy of Co-based 3*d* transition-metal thin films is systematically investigated. The computational results predict that large perpendicular magnetocrystalline anisotropy can be achieved by tuning the atomic-layer alignments in Ni-Co thin film. I discovered that not only the on-site SOC of 3*d* elements determines the magnetocrystalline anisotropy energy but also the strong hybridization between these elements plays a constructive role to enhance the perpendicular magnetocrystalline anisotropy. An external electric field is applied as sawtooth-like potentials, which have the right periodicity but which represent unrealistic, discontinuous electric fields. The effect of the

electric field, however, does not give any manipulation to the magnetocrystalline anisotropy in Co-based thin film.

In Chapter 4, the magnetic properties and the effect of electric fields in two-dimensional magnetic bilayer materials, CrI_3 and VI_3, were investigated. The crystal-field in the iodine octahedra splits $3d$ orbital states into two-fold e_g and three-fold t_{2g} states; the latter level is further split into a singlet a_{1g} and a doublet e'_g by trigonal distortion. In VI_3, Jahn-Teller distortion makes the empty a_{1g} state play an important role to open the band gap and determine the inter-layer magnetic interaction. Moreover, calculations were performed for two different stacking of bilayer VI_3 in which the electric fields were applied perpendicular to the slab. The results predict that the magnetic stability of the bilayer VI_3 can be tuned by the external electric fields, which is comparable with the case of bilayer CrI_3. The magnetic phase transition can be explained by the virtual hopping mechanism.

Finally, I summarize this thesis in Chapter 5.

Chapter 2

Theoretical background

2.1 Density functional theory

2.1.1 Introduction

Density functional theory (DFT) has become the primary tool for the calculation of electronic structure in condensed matter and is increasingly important for quantitative studies of molecules and other finite systems. This is a theory of correlated many-body systems, and because the particles are so light, quantum mechanics is needed: a quantum many-body problem. Thus our standing point is the Hamiltonian for the system of electrons and nuclei,

$$H = -\frac{\hbar^2}{2m_e}\sum_i \nabla_i^2 - \frac{\hbar^2}{2}\sum_i \frac{\nabla_I^2}{M_I} - \sum_{i,I}\frac{Z_I e^2}{|\mathbf{r}_i - \mathbf{R}_I|} + \frac{1}{2}\sum_{i\neq j}\frac{e^2}{|\mathbf{r}_i - \mathbf{r}_j|} + \sum_{I\neq J}\frac{Z_I Z_J e^2}{|\mathbf{R}_I - \mathbf{R}_J|} \tag{2.1}$$

The mass of the nucleus at $\mathbf{R}_I$ is M_I, the electrons at $\mathbf{r}_i$ have mass m_e. The first term in Eq. 2.1 is the kinetic energy for the electrons, the second term is for the nuclei. The last three terms describe the Coulomb interaction between electrons and nuclei, between electrons and other electrons, and between nuclei and other nuclei. It is out of the question to solve this problem exactly.

First-principles electronic structure calculations are based on DFT using the fundamental constants of physics as input to provide detailed insight into the origin of electronic structure, magnetic properties, mechanical and optical properties of materials. Starting from first-principles, equations are derived under some approximations and solved for a realistic system. The methods do not require any experimental parameters and knowledge and also do not depend on material systems. From first-principles, one may predict properties to be

compared with experiments, understand the underlying microscopic mechanism, and design new materials with desired properties.

2.1.2 The Hohenberg-Kohn theorem

The nuclei are much heavier and therefore much slower than the electrons. Since the nuclei do not move anymore, their kinetic energy is zero and the second term disappears. The last term reduces to a constant. We are left with the kinetic energy of the electron gas, and the potential energy due to electron-electron interactions, and the potential energy of the electrons in the potential of nuclei. Hence, Hohenberg and Kohn [5] established the DFT in which the many body system can be expressed in terms of single-particle equation. The formulation applies to any systems of interacting particles with an external potential $V_{ext}(\mathrm{r})$, where the Hamiltonian be written as

$$H = T + U + V = -\frac{\hbar^2}{2m_e}\sum_i \nabla_i^2 + \frac{1}{2}\sum_{i\neq j}\frac{e^2}{|\mathbf{r}_i - \mathbf{r}_j|} + \sum_i V_{ext}(\mathbf{r}_i),$$

The first term is the kinetic energy, the second term is the interaction with the external potential and the third term is the electron-electron Coulomb repulsion. The quantum many body problem obtained after the first level approximation is much simpler than the original one, but still far too difficult to solve. DFT, one of the most modern and powerful methods, is based upon two theorems due to Hohenberg and Kohn.
The first theorem is: *The external potential $V_{ext}(\mathbf{r})$ is determined uniquely by the ground state particle density $n_0(\mathbf{r})$.*

$$E[n] = F[n] + \int V_{ext} n(\mathbf{r})\, d\mathbf{r}, \tag{2.2}$$

$$F[n] = \langle \psi | T + U | \psi \rangle$$

This theorem states that if the electron density $n_0(\mathbf{r})$ is given, all properties of the system are completely determined.

The second theorem is: *For any given $V_{ext}(\mathbf{r})$, the correct ground state energy of the system is the global minimum value of the energy functional.*

The Hohenberg-Kohn arguments are very general for properties of interacting particle systems, yet the special emphasis is on the ground state. Nevertheless, it is difficult to fulfill all the properties guaranteed by the Hohenberg-Kohn because no one has found a way to extract directly from the density any general set of properties, e.g whether the material is a metal or insulator. The key point is that the density is an allowed density of quantum

mechanical systems, it is this fact that builds in the quantum effects. The difficulty can be illustrated by considering a case where the exact solution can be found – N non-interacting electrons in an external potential. This is the central problem in the Kohn-Sham approach to the DFT.

2.1.3 The Kohn-Sham equation

The equations of Kohn and Sham, published in 1965, turn DFT into a practical tool [6]. The problem of finding the ground state is reduced to solving one-partical equations. Since there is no unique prescription for choosing the simpler auxiliary system, they can assume that the ground state density of the original interacting system is equal to that of some chosen non-interacting system. This leads to independent-particle equations for the non-interacting system that can be considered exactly soluble with all the difficult many-body terms incorporated into an exchange-correlation functional of the density. The corresponding Hamiltonian – called the Kohn-Sham Hamiltonian as

$$H_{\mathrm{KS}} = -\frac{\hbar^2}{2m}\sum_i \nabla^2 - V_{ext}(\mathbf{r}) + e^2 \int \frac{n(\mathbf{r}')}{|\mathbf{r}-\mathbf{r}'|}\, d\mathbf{r}' + V_{xc}(n(\mathbf{r})), \tag{2.3}$$

The theorem of Kohn and Sham can now be formulated as follows: The exact ground-state density $n(\mathbf{r})$ of an N-electron system is

$$n(\mathbf{r}) = \sum_j |\psi_j(\mathbf{r})|^2, \tag{2.4}$$

and the exchange-correlation potential defined as

$$V_{\mathrm{xc}} = \frac{\delta E_{\mathrm{xc}}[n(\mathbf{r})]}{\delta n(\mathbf{r})}, \tag{2.5}$$

The last two terms in Eq. 2.3 are the classical Hartree term and the exchange-correlation term. These two terms depend on the electron density $n(\mathbf{r})$, which in turn depends on the $\psi_j(\mathbf{r})$ (which are being searched). This means we are dealing with a self-consistency problem: the solution of $\psi_j(\mathbf{r})$ determine the original equation, and the equation cannot be written down and solved before its solution is known.

2.1.4 Generalized gradient approximation

In order to solve the Kohn-Sham equation in practice, I introduce the generalized gradient approximation (GGA)

$$E_{\mathrm{xc}}[n] = \int \varepsilon_{\mathrm{xc}}\left(n(\mathbf{r}), \nabla n(\mathbf{r})\right) d\mathbf{r}, \tag{2.6}$$

where $\varepsilon_{\mathrm{xc}}(n(\mathbf{r}), \nabla n(\mathbf{r}))$ is the exchange-correlation energy as a functional of density $n(\mathbf{r})$ and density gradient $\nabla n(\mathbf{r})$. So that, the exchange-correlation potential given as follows

$$V_{\mathrm{xc}}(\mathbf{r}) = \left[\varepsilon_{\mathrm{xc}} + n\frac{\delta E_{\mathrm{xc}}}{\delta n^{\sigma}} - \nabla\left(n\frac{\delta E_{\mathrm{xc}}}{\delta \nabla n^{\sigma}}\right)\right]_{\mathbf{r},\sigma}, \tag{2.7}$$

Useful estimates of numerous form is illustrated by three widely used forms of Becke (B88) [7] , Perdew and Wang (PW91) [8], and Perdew, Burke, and Enzerhof (PBE) [9]. Among them, the PBE form is the most useful as the simplest GGA functional.

2.2 Relativistic effects

2.2.1 Dirac equation

Let's start with the idea to create a relativistic wave equation for free particle related to the Schrödinger equation by Klein and Gordon (1926) as [10, 11],

$$-\hbar^2\frac{\partial^2\Psi}{\partial^2 t} = -\hbar^2c^2\nabla^2\Psi + m^2c^4\Psi, \tag{2.8}$$

by promoting the energy operator E and momentum operator p into the relativistic energy–momentum relation

$$E^2 = p^2c^2 + m^2c^4, \tag{2.9}$$

The Dirac equation is introduced, following the original work of Dirac (1928) [12], as a factorization of Eq. 2.8. The Dirac equation in its Hamiltonian form is given as,

$$i\hbar\frac{\partial}{\partial t}\Psi = H\Psi \tag{2.10}$$

with

$$H = c\alpha\cdot\mathbf{p} + \beta mc^2 \tag{2.11}$$

where Ψ is a time-dependent four-component single particle wave function and H is the single-particle Hamiltonian. The quantity α is a vector operator whose components can be

written as,

$$\alpha = \begin{pmatrix} 0 & \sigma_k \\ \sigma_k & 0 \end{pmatrix}, \tag{2.12}$$

σ_k is the Pauli spin matrices, where in the standard representation,

$$\sigma_1 = \begin{pmatrix} 0 & 1 \\ 1 & 0 \end{pmatrix}, \sigma_2 = \begin{pmatrix} 0 & -i \\ i & 0 \end{pmatrix}, \sigma_3 = \begin{pmatrix} 1 & 0 \\ 0 & -1 \end{pmatrix}$$

are the x, y and z Pauli spin matrices. The quality $\mathbf{p}$ is the momentum operator, $\mathbf{p} = -ih\nabla$ and the matrix β is given by,

$$\beta = \begin{pmatrix} \mathbf{1} & 0 \\ 0 & -\mathbf{1} \end{pmatrix}, \tag{2.13}$$

with

$$\mathbf{1} = \begin{pmatrix} 1 & 0 \\ 0 & 1 \end{pmatrix} \tag{2.14}$$

In presence of an electromagnetic field, by substituting the Gauge-invariant

$$i\hbar\frac{\partial}{\partial t} \rightarrow i\hbar\frac{\partial}{\partial t} - e\Phi(\mathbf{r},t) \tag{2.15}$$

$$-i\hbar\nabla \rightarrow -i\hbar\nabla - e\mathbf{A}(\mathbf{r},t) \tag{2.16}$$

into Eq. 2.11 we obtain

$$i\hbar\frac{\partial}{\partial t}\Psi = \left(\alpha\cdot(c\mathbf{p} - e\mathbf{A}) + \beta mc^2 + e\Phi\right)\Psi \tag{2.17}$$

where $\mathbf{A}$ is the vector potential and Φ is the scalar potential.

2.2.2 The fine structure Hamiltonian

Now I focus on the fine structure case of the hydrogen atom model without external magnetic field. The target is to find a kind of the relativistic correction to the non-relativistic Schrödinger equation. From Eq. 2.17, the fine structure Hamiltonian can be obtained via a direct approach and perturbation theory, is described as

$$H = \frac{\mathbf{p}^2}{2m} + V - \frac{\mathbf{p}^4}{8m^3c^2} - \frac{\hbar^2}{4m^2c^2}\frac{dV}{dr}\frac{\partial}{\partial r} + \frac{1}{2m^2c^2r}\frac{dV}{dr}\mathbf{S}\cdot\mathbf{L} \tag{2.18}$$

where $V = e\Phi$ is the central potential, $\mathbf{L} = \mathbf{r} \times \mathbf{p}$ is the angular momentum and $\mathbf{S} = \frac{\hbar}{2}\sigma$ is electron spin.

The first two terms in Eq. 2.18 come from the Schrödinger equation and the rest of the terms are the corrections. The third term is the natural relativistic correction of the energy linked to the approximation of the relativistic energy. The fourth term is Darwin term and it can be interpreted as an effective smearing out of the potential due to the lack of localization of the electron. The last term in Eq. 2.18 takes into account the coupling between the spin and the orbital angular momentum, it is the spin-orbit coupling (SOC). This term is generally known as,

$$H_{\mathrm{SOC}} = \xi \mathbf{S} \cdot \mathbf{L} \tag{2.19}$$

where ξ is called the spin-orbit parameter.

2.2.3 Magnetocrystalline anisotropy

The spin-orbit coupling describes the coupling between the spin and the orbital angular momentum. The SOC is much smaller than the exchange interaction, however, it plays a crucial role in the magnetic system. One of the important features of the SOC is the origin of the magnetocrystalline anisotropy, which is a key parameter in spintronics devices.

Now let us simplify Eq. 2.18 into the simply two-component Pauli equation as,

$$(H_{\mathrm{scalar}} + H_{\mathrm{SOC}})\Psi_n^{\mathbf{k}}(\mathbf{r}) = \varepsilon_n^{\mathbf{k}}(\mathbf{r})\Psi_n^{\mathbf{k}}(\mathbf{r})(\mathbf{r}), \tag{2.20}$$

where the Hamiltonian has been split into a spin-polarized scalar-relativistic part H_{scalar}, including the mass-velocity and Darwin terms and will be treated fully self-consistently, and the spin-orbit interaction, which will be added in the last iteration of the self-consistent field procedure. To calculate the magnetocrystalline anisotropy, I start from a self-consistent spin-polarized scalar-relativistic calculation, then adding H_{SOC} to H_{scalar} and solving the corresponding Kohn-Sham Eq. 2.20 non-self-consistently(see A, B). Assuming that the self-consistent calculation with H_{scalar} is so close to self-consistency, the change in the total energy with a chosen magnetization direction is given by the change in the single-particle eigenvalue sum:

$$\Delta E = \sum_{i,\mathbf{k}}^{\mathrm{occ}} \varepsilon_i(\mathbf{n},\mathbf{k}) - \sum_{i,\mathbf{k}}^{\mathrm{occ}} \varepsilon_i(\mathbf{k}) \tag{2.21}$$

where $\mathbf{n}$ is an arbitrarily chosen magnetization direction and $\varepsilon_i(\mathbf{n},\mathbf{k})$ is the energy eigenvalues over k-space. This relation has been called the force theorem, which is firstly proposed by

Weinert *et al.* (1985) [13]. The magnetocrystalline anisotropy energy (MAE) is obtained from the energy eigenvalue difference for the magnetization oriented along the hard-axis and easy-axis, can be written as

$$\begin{aligned} MAE &\equiv \Delta E(\mathbf{n_1},\mathbf{n_2}) \\ &= \Delta E(\mathbf{n_1}) - \Delta E(\mathbf{n_2}) \\ &= \sum_{i,\mathbf{k}}^{\text{occ}} \varepsilon_i(\mathbf{n_1},\mathbf{k}) - \sum_{i,\mathbf{k}}^{\text{occ}} \varepsilon_i(\mathbf{n_2},\mathbf{k}). \end{aligned} \tag{2.22}$$

2.3 External electric field

2.3.1 Inclusion of a static external field

To perform first-principles calculations in an electric field it would seem that I only need to add a term of the form as

$$\int V_{\text{ext}}(\mathbf{r}) n(\mathbf{r})\, d\mathbf{r}, \tag{2.23}$$

to the energy functional, where V_{ext} is the potential associated with the field. An external field and its corresponding potential can be related to a charge distribution $\rho_{\text{ext}}(\mathbf{r})$ via Poisson's equation

$$\nabla^2 V_{\text{ext}}(\mathbf{r}) = -4\pi\rho_{\text{ext}}(\mathbf{r}). \tag{2.24}$$

The density and potential can be describe the in a two-dimensional Fourier expansion as,

$$V(\mathbf{r}) = \sum_{\mathbf{G}_\parallel} V(\mathbf{G}_\parallel, z) \mathrm{e}^{i\mathbf{G}_\parallel \cdot \mathbf{r}_\parallel}. \tag{2.25}$$

In this representation, the Poisson equation is separated into

$$\left[\frac{\partial^2}{\partial z^2} - \mathbf{G}_\parallel^2\right] V(\mathbf{G}_\parallel, z) = -4\pi\rho(\mathbf{G}_\parallel, z). \tag{2.26}$$

For the uniform field ($\mathbf{G}_\parallel$), two boundary conditions are required to specify the solution of Eq. 2.26. Integrating this equation, using mixed boundary conditions at $z = z_0 (z < z_0)$, gives the potential in terms of the density as

$$V(z) = V(z_0) - (z_0 - z)\left(\frac{\partial}{\partial z}V(z)|_{z=z_0}\right) - 4\pi\int \rho(z')(z'-z)\,dz'. \tag{2.27}$$

Because of the linearity of Poisson's equation, one might be free to pick these boundary conditions in any convenient manner. The problem is that in our framework the Hamiltonian needs to have the same periodicity as the system. Hence, saw-like potentials are used to deal with the periodic systems (see figure 2.1). The dipole correction will be introduced to solve the periodic boundary problem in the vacuum region.

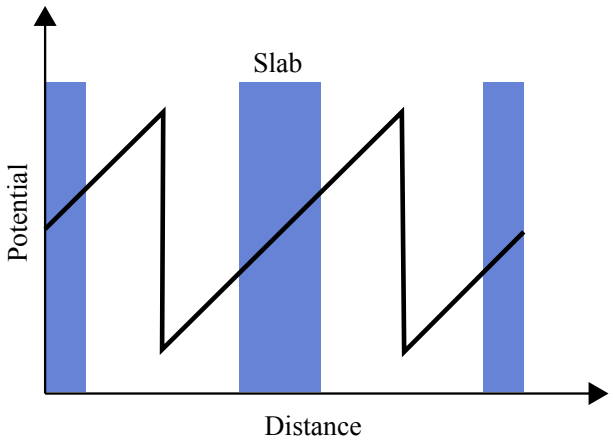

Fig. 2.1 Electric field is applied by the saw-like potential in slab structure because of the periodic boundary condition.

2.3.2 Dipole correction

The periodic boundary conditions imposed on the electrostatic potential then give rise to an artificial electric field across the slab. To cancel the artificial field, one needs to introduce a dipole correction in the vacuum region of the supercell [14, 15].

For more convenient discussion, let's separate Eq. 2.27 into two parts as follows:

$$V'(z) = V(z_0) - (z_0 - z)\left(\frac{\partial}{\partial z}V(z)|_{z=z_0}\right), \tag{2.28}$$

and

$$V_{\text{avg}}(z) = -4\pi\int \rho(z')(z'-z)\,dz'. \tag{2.29}$$

Now assuming that the slab is put in a box of height z_m with periodic boundary conditions also in the z direction. Because $V'(\mathbf{r})$ decays exponentially away from the surface, the error

made when imposing periodic boundary conditions on V' should be small. On the other hand, V_{avg} has emerged in the laterally averaged part of the potential:

$$V_{\text{avg,per}}(z) = V_{\text{avg}}(z) - 4\pi m \left(\frac{z}{z_m} - \frac{1}{2} \right), \tag{2.30}$$

where

$$m = \int \rho(z')(z' - z)\, dz'. \tag{2.31}$$

in order to satisfy $V_{\text{avg,per}}(0) = V_{\text{avg,per}}(z_m)$. An approximation for the Hartree potential of the isolated slab is thus

$$V(\mathbf{r}) \approx V_{\text{per}}(\mathbf{r}) + V_{\text{dip}}(z), \tag{2.32}$$

where

$$V_{\text{dip}}(z) = 4\pi m \left(\frac{z}{z_m} - \frac{1}{2} \right), 0 < z < z_m. \tag{2.33}$$

is the dipole correction with the associated energy

$$E_{\text{dip}} = \frac{1}{2} \int \rho(\mathbf{r}) V_{\text{dip}}(z)\, d^3 r. \tag{2.34}$$

The potential term V_{dip} corresponds to an electric field $E_z = -4\pi m / z_m$. The energy associated with the dipole correction field differs from the energy shift caused by an external applied electric field by a a factor of 1/2, which is explained by the fact that the dipole correction field has an internal origin.

2.4 Strongly correlated electron systems

2.4.1 Classical spin models

The spin Hamiltonian depends on the spin contributions and spin properties of the system and enumerates the orbital momentum contributions required to define the system. The total Hamiltonian for a magnetic system is the sum of all these magnetic interactions:

$$H = H_{\text{exc}} + H_{\text{ani}} + H_{\text{dip}} + H_{\text{DMI}} + H_{\text{ext}}, \tag{2.35}$$

where the Hamiltonian includes the isotropic exchange interaction, the magnetic anisotropy, the dipolar interactions, the Dzyaloshinskii-Moriya interactions and the Zeeman interaction.

The classical Heisenberg Hamiltonian with the nearest-neighbor exchange interaction reads

$$H_{\text{exc}} = \sum_{\langle i,j \rangle} J_{ij} \mathbf{S}_i \cdot \mathbf{S}_j, \tag{2.36}$$

where J_{ij} is an isotropic exchange interaction between the spin vectors when each pair of spins ($\mathbf{S}_i$, $\mathbf{S}_j$) has been counted only once. Since I consider the relative orientation of both the spins, the interaction can be considered as isotropic.

The second term in Eq.2.35 represents the magnetocrystalline anisotropy (MA) with the dominant contribution from the uniaxial anisotropy as,

$$H_{\text{ani}} = K_u \sum_i (\mathbf{S}_i \cdot \mathbf{u})^2, \tag{2.37}$$

with K_u as the anisotropy constant in eV and easy axis along the unitary $\mathbf{u}$ direction.

The third term in Eq.2.35 is the dipole-dipole interaction defined as

$$H_{\text{dip}} = -\frac{\mu_0 \mu_s^2}{4\pi} \sum_{i<j} \frac{3(\mathbf{S}_i \cdot \mathbf{r}_{ij})(\mathbf{S}_j \cdot \mathbf{r}_{ij}) - \mathbf{S}_i \cdot \mathbf{S}_j}{r_{ij}^3}, \tag{2.38}$$

with $\mathbf{r}_{ij}$ is the spatial vector pointing from the i^{th} to the j^{th} lattice site. The dipole-dipole interaction is long range and can be neglected in studies of short wave length excitations. The Dzyaloshinskii-Moriya interaction (H_{DMI}) in Eq.2.35 is an antisymmetric, anisotropic exchange coupling between two neighboring magnetic spins $\mathbf{S}_i$ and $\mathbf{S}_j$

$$H_{\text{DMI}} = \sum_{\langle i,j \rangle} \mathbf{D}_{ij} \cdot [\mathbf{S}_i \times \mathbf{S}_j], \tag{2.39}$$

And the last term in Eq.2.35 is the Zeeman energy describing the interaction of the magnetic system with an external magnetic field. The Zeeman energy is,

$$H_{\text{ext}} = -\mathbf{B}_{\text{ext}} \sum_i \mathbf{S}_i, \tag{2.40}$$

2.4.2 Hubbard model

Strong correlations between electrons (e.g., the interaction of conduction electrons with almost localized magnetic moments) can cause various outstanding features such as superconductivity or insulating ground state with ferromagnetic. Hubbard model was proposed in

1963 to describe strongly correlated electrons in 3d transition metals [16]. In these elements, the radial wave function of the $3d$-electrons has a very small spatial extent. Thus, when the 3d shell is occupied by several electrons, these are forced to be close to one another on the average so that the electrostatic energy is large. The energy of a given transition metal ion, therefore, varies strongly with the number of electrons it contains. The model thus can be written as

$$H = -t \sum_{\langle i,j \rangle,\sigma} c^{\dagger}_{i\sigma} c_{j\sigma} + U \sum_{i} n_{i\uparrow} n_{i\downarrow}, \tag{2.41}$$

The first term of Eq. 2.41 is the hopping of electrons from site to site, where $c^{\dagger}_{i\sigma}$, $c_{i\sigma}$ are creation and annihilation operators of electrons at site i with spin σ, and t is the hopping matrix elements. The second term of Eq. 2.41 is the on-site Coulomb repulsion of two electrons at site i. This interaction contains the electron densities at each site i, $n_{i\sigma} = c^{\dagger}_{i\sigma} c_{i\sigma}$ with opposite spin and the energy of Coulomb repulsion of two electrons at site i, U. Fig. 2.2 illustrates the Coulomb energy U and the hopping t in the Hubbard model. There are three possible hopping processes can be considered in this model: hopping of electron from the occupied to the neighbouring empty site, virtual hopping of electron from the occupied to the neighbouring site and back, and the three-process hopping. In Fig. 2.3, I introduce the virtual hopping, which will be used for the main discussion in Chapter 4. Considering the Hubbard model as Eq. 2.41 with one electron per site ($n = 1$) and strong correlation $U \gg t$, there are two situations;

1. If the spins are anti-parallel, electron hopping (first term in Eq. 2.41) is allowed to move an electron from one site to a neighboring site. And in principle, second-order process is possible to move that electron back. The energy gain is this process is $-2t^2/U$.

2. If the spins are parallel, the above process is forbidden by the Pauli exclusion principle, no energy gain.

2.5 Wannier functions

2.5.1 Bloch functions and Wannier functions

Periodic boundary conditions are widely used in electronic structure calculation using the set of extended Bloch states

$$\psi_{n\mathbf{k}}(\mathbf{r}) = u_{n\mathbf{k}}(\mathbf{r}) e^{i\mathbf{k}\cdot\mathbf{r}}, \tag{2.42}$$

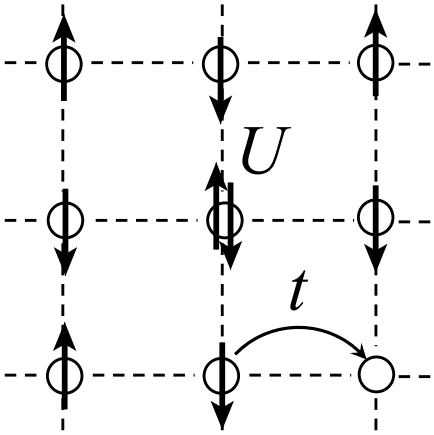

Fig. 2.2 Hubbard model with U is the Coulomb repulsion energy of electrons in one site and t is the hopping of electrons between two sites.

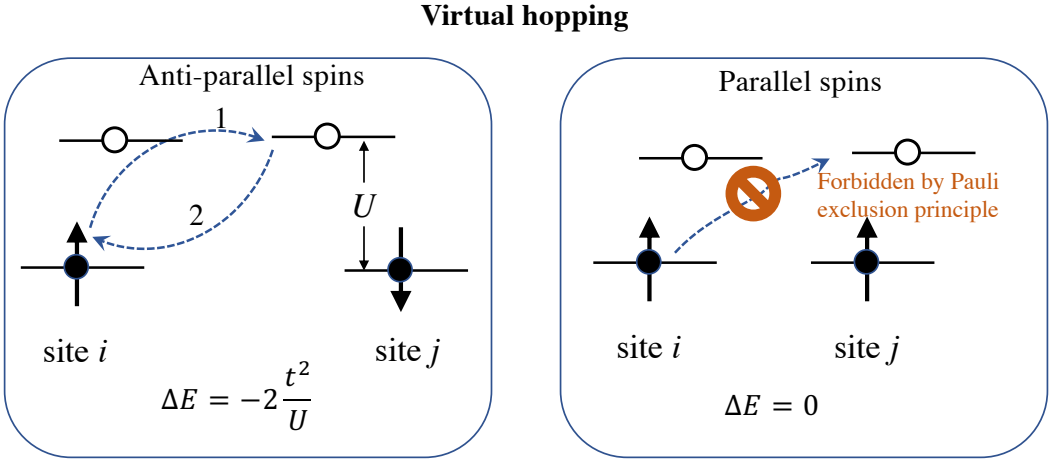

Fig. 2.3 Virtual hopping in the case of parallel and anti-parallel spins when I consider the Hubbard model with one electron per site.

where n is the band index and the lattice-periodic parts $u_{n,\mathbf{k}}(\mathbf{r})$ is periodic in real space with respect to the unit cell of the crystal. Thus, Bloch functions are oscillating and delocalized in real space. However, orbitals that are localized in real space offer a microscopic understanding of the physical processes. To deal with this matter, Wannier (1937) [17] proposed an alternative representation, in which the Bloch states is expressed in terms of a Fourier series as

$$\psi_{n\mathbf{k}}(\mathbf{r}) = \sum_{\mathbf{R}} e^{i\mathbf{k}\cdot\mathbf{R}} W_{n\mathbf{R}}(\mathbf{r}), \tag{2.43}$$

where $\mathbf{R}$ is a real-space lattice vector. The inverse of this series leads to so-called Wannier functions (WFs) that are Fourier transformations of the original Bloch states:

$$W_{n\mathbf{R}}(\mathbf{r}) = \frac{1}{N}\sum_{\mathbf{k}} e^{-i\mathbf{k}\cdot\mathbf{R}} \psi_{n,\mathbf{k}}(\mathbf{r}). \tag{2.44}$$

The transformations of Eq. 2.43 and Eq. 2.44 create a unitary transformation between Bloch states and Wannier states. This means that any Bloch functions on the $\mathbf{k}$ space can be built up by superposing the WFs linearly. Even they are not eigenstates of the single-particle Hamiltonian, the WFs are practically useful in studying intrinsic properties of materials.

2.5.2 Gauge freedom

The phases of the Bloch functions in are not unique and can be twisted by a gauge change as

$$|\tilde{u}_{n\mathbf{k}}\rangle = e^{-i\beta(\mathbf{k})}|u_{n\mathbf{k}} \tag{2.45}$$

where $\beta(\mathbf{k})$ is some real function of $\mathbf{k}$. Each gauge transformation is invariant under a translation by $\mathbf{G}$ as periodic condition

$$\beta(\mathbf{k}+\mathbf{G}) = \beta(\mathbf{k}) + \mathbf{G}\cdot\mathbf{R} \tag{2.46}$$

Since the transformation preserves the periodic property, the center of charge of WFs are gauge-invariant and simply shifted by a lattice vector. This means that all choice of gauge lead to the same Wannier center and the same energy-band coefficients. However, it is not true that all WFs are created equal with different choice of gauge. In the Fourier transforms, the smooth gauge we chose in the reciprocal space leads to the more localized function in the real space. Hence, different choices of smooth gauge correspond to different sets of WFs (shapes and spreads, in general).

2.5.3 Multiband Wannier functions

Before discussing how to constructing a smooth gauge, let assume that $\psi_{n\mathbf{k}}$ is smooth and periodic over the $\mathbf{k}$ space. Since it is hard to treat the condition that n band be a single isolated band, one need to consider a manifold of M band that are glued together by degeneracies. This band manifold are invariant under any unitary transformation of the form

$$|\tilde{\psi}_{n\mathbf{k}}\rangle = \sum_{m=1}^{M} U_{mn}(\mathbf{k})|\psi_{m\mathbf{k}} \tag{2.47}$$

where $|\tilde{\psi}_{n\mathbf{k}}\rangle$ is Bloch-like functions that are smooth functions everywhere in the $\mathbf{k}$ space. U_{mn} is a manifold of $M \times M$ unitary matrices whose is periodic in $\mathbf{k}$. Noting that the $|\psi_{n\mathbf{k}}\rangle$ and $|u_{n\mathbf{k}}\rangle$ transform in the same way, one may rewrite Eq. 2.47 as

$$|\tilde{u}_{n\mathbf{k}}\rangle = \sum_{m=1}^{M} U_{mn}(\mathbf{k})|u_{m\mathbf{k}} \tag{2.48}$$

2.5.4 Wannier functions via projection

A simple and effective approach for constructing a smooth gauge in $\mathbf{k}$ for a corresponding set of well-localized WFs is by projection. Starting from a set of chosen trial orbitals $g_n(\mathbf{r})$ which correspond to some rough guess for the WFs, one may project these $g_n(\mathbf{r})$ orbitals onto the Bloch manifold at the wave vector $\mathbf{k}$ to obtain [18]

$$|\phi_{n\mathbf{k}}\rangle = \sum_{m=1}^{M} |\psi_{m\mathbf{k}}\rangle\langle\psi_{m\mathbf{k}}|g_n\rangle, \tag{2.49}$$

where M is the number of trial orbitals. The overlap matrix over one cell is defined as

$$(S_{\mathbf{k}})_{mn} = \langle\phi_{m\mathbf{k}}|\phi_{n\mathbf{k}}\rangle, \tag{2.50}$$

Then, one can construct the Bloch-like states as

$$|\tilde{\psi}_{n\mathbf{k}}\rangle = \sum_{m=1}^{M} |\phi_{m\mathbf{k}}\rangle(S_{\mathbf{k}}^{-1/2})_{nm}. \tag{2.51}$$

where $|\tilde{\psi}_{n\mathbf{k}}\rangle$ are uniquely defined by the trial orbitals $g_n(\mathbf{r})$ and related to the original $|\psi_{n\mathbf{k}}\rangle$ by a "gause transformation" as

$$|\tilde{\psi}_{n\mathbf{k}}\rangle = \sum_{m=1}^{M} U_{nm}^{(\mathbf{k})}|\psi_{m\mathbf{k}}\rangle \tag{2.52}$$

where $U_{nm}^{(\mathbf{k})}$ is a unitary matrix and has a periodicity in $\mathbf{k}$. After the electronic-structure calculations has been self-consistently converged and a set of ground-state Bloch orbitals has been chosen, the unitary matrix is refined.

2.5.5 Maximally localized Wannier functions

A very general approach for constructing a well-defined localized Wannier functions was developed by Marzari and Vanderbilt (1997) [18], namely Maximally localized Wannier functions (MLWFs). The well-localzied functions are obtained by minimizing the localization functional concerning the $U_{nm}^{(\mathbf{k})}$ appearing. The localization functional is described as

$$\Omega = \sum_{n} \left[\langle \mathbf{0}n|r^2|\mathbf{0}n\rangle - \langle \mathbf{0}n|\mathbf{r}|\mathbf{0}n\rangle^2 \right] \tag{2.53}$$

measuring the sum of spreads of the M WFs around their centers. Now let consider a finite chanin cut form the infinite system to define Wannier-like localized functions. Suppose that the segment consisting of L unit cells having M occupied bands. Then $N = ML$ is the number of occupied states. Now we can construct the $N \times N$ matrix from the N eigenstates $|\varphi_i\rangle$

$$V_{ij} = \langle \varphi_i|x|\varphi_j\rangle \tag{2.54}$$

and obtain its eigenvalues $\bar{x}$. The total spreads of these functions can be expressed as

$$\Omega_{\text{spread}} = \sum_{i=1}^{N} \left[\langle \varphi_i|x^2|\varphi_i\rangle - \langle \varphi_i|x|\varphi_i\rangle^2 \right] \tag{2.55}$$

The first term in Eq. 2.55 is a trace over the occupied subspace of the x^2 operator and is invariant to the choice of unitary rotation. Therefore, it can be dropped. So we can minimize the spread by minimizing the sum of squares $\sum_i \langle \varphi_i|x|\varphi_i\rangle^2 = \sum_i {V_{ii}}^2$ of the orbital centers.

In this work, the MLWFs are used in constructing localized molecular orbitals and estimating hopping integral for strongly correlated systems.

2.5.6 Wannier functions as a basis for strongly correlated systems

For many strongly correlated electron problems, the essential physics of the system can be explained by considering WFs. One can express the Hubbard model (Eq. 2.41) in term of a complete tight-binding basis as

$$H = -t_{ij} \sum_{\langle i,j\rangle,\sigma} c^{\dagger}_{i\sigma} c_{j\sigma} + U \sum_{i} n_{i\uparrow} n_{i\downarrow}, \tag{2.56}$$

where i, j labels the correlated site. The single-particle hopping parameters t of the model Hamiltonian are easily obtained from the matrix elements of the DFT Hamiltonian represented based on MLWFs as

$$t_{ij} = \langle W_i | H | W_j \rangle \tag{2.57}$$

According to Anderson (1959) [19], the exchange interaction processing based on hopping parameter can be expressed as

$$J^{kin}_{ij} = \frac{2t^2_{ij}}{U}. \tag{2.58}$$

Chapter 3

Electric field effect on magnetic anisotropy in transition metal thin films

3.1 Introduction

Magnetic random access memory (MRAM) has been seriously considered to replace other traditional random access memory devices in the next generation owing to the fast, long-service-life, low-power-consuming, and non-volatile properties [20–22]. For the practical application, magnetic atomic layers that exhibit strong perpendicular magnetocrystalline anisotropy (PMA) are desired to enhance the potential of high-density MRAM as they have high thermal stability and low critical current for current-induced magnetization switching [23]. To this end, transition-metal thin films such as (Co, Fe)/(Pd, Pt) [24–26] multilayers and (Fe, CoFeB)/MgO [27, 28] thin films have been proposed to exhibit PMA. While enhancement of the PMA in transition-metal films is crucially required, its realization is not straightforward. It has been known that the MA microscopically results from on-site SOC. Perturbation theory of SOC with the crystal-field $3d$ states deduces the fact that MAE is proportional to the SOC-induced orbital magnetic moment as proposed by Bruno [29]. The so-called “Bruno’s theory" has been confirmed in several magnetic multilayers [30–32]. However, in the materials where hybridization between different elements is strong enough, the MAE is not simply the summation of the on-site SOC energy, but a cross term between the SOC matrix elements and the hybridization plays a more important role. Indeed, the MAE is determined not only by the choice of atomic elements but also on the detail of the atomic layer alignment in multilayers composed of several types of atoms [33, 34]. Moreover, a modification in the MAE, with the application of an external electric field was observed in several thin film systems [35–38]. The effect of electric field on the MAE may give an

potential application in spintronics field. Motivated by these findings, I theoretically design a rather simple system based on Co-based artificial multilayers with Ni, Fe, and Mn, evaluate the MAE, and discuss which ingredient may enhance the MAE and the electric field effect by using the first-principles approach.

In this chapter, I show the results of MAE calculation in Co-based 3*d* transition-metal thin films. The calculations were done for five- and seven-layer slab of films for hexagonal close-packed (hcp) and face-centered cubic (fcc) stacking. The results of pure Co thin films are shown to consider the MAE and the stability between hcp and fcc stacking. In the next session, the MAE calculations of five atomic-layer Co-based 3d elements (Ni, Fe, Mn) films are shown. In the final session, the MAE calculations of seven atomic-layer Co-based 3*d* elements films are shown. The DOS and band structure are presented to discuss the mechanism of MA for all systems. The electric field effect on the MAE is also provided in the last part of this chapter.

3.2 Computational methods

I performed first-principles DFT calculations by using the highly precise full-potential linearized augmented plane-wave (FLAPW) method [39, 40] based on the generalized gradient approximation (GGA) [9] to DFT implemented in the HiLAPW code [41]. SOC is taken into account for the valence and core states by the second-variation method [42]. The energy cutoffs of 20 and 160 Ry were used for wave function expansions and potential representations. Muffin-tin sphere radii of 1.9 a.u for Co, Fe, Ni, Mn are used and the Soler-Williams type augmentation method [43] was adopted. Calculations were performed in a three-step flow. First, structure optimizations were performed for the atomic coordinates until the force become lower than 1 meV/Å for determining the most stable interfacial geometries. A $22\times22\times1$ k-mesh in the two-dimensional Brillouin zone was used for the structure optimization. In the second step, the Kohn-Sham equations are solved without SOC taken into account to determine the charge distribution of the ground state. Finally, the SOC is introduced by the second-variation method. The MAE is evaluated by the force theorem [13, 44, 45] as defined as the eigenvalue-sum difference between the in-plane and perpendicular magnetic directions: $E_{\mathrm{MA}} = E_{\mathrm{in}} - E_{\mathrm{perp}}$ in the cell. It was checked that the use of 5184 special k points was sufficient to suppress numerical fluctuations in the calculated MAE values. Electric field is applied perpendicular to the surface by saw-like potential with dipole correction [14, 15].

3.3 Model of Calculations

Calculations were carried out for five- and seven-layered slabs of Co-based transition-metal thin films whose both sides are terminated by Co layers as being consistent with the experimental setting [24], in which Co layers on Pt fcc lattice are synthesized and grow up in either hcp (0001) or fcc (111) stacking as depending on the film thickness and the location. In our calculations, both hcp-like (ABAB) and fcc-like (ABCABC) stacking are considered and the total-energy difference between them is evaluated as the structural stability. Iconsidered three (i-iii) and six (I-VI) possible atomic-layer alignments for five- and seven-layered slabs, respectively, with Co and other 3*d* elements, i.e. Ni, Fe, and Mn (see Fig. 3.1). The in-plane lattice constant $a = 2.7918$Å is assumed to match the experimental value of Pt (111) and the vacuum layer is assumed to be $\sim$8.5Å which is large enough for transition-metal thin-film calculations.

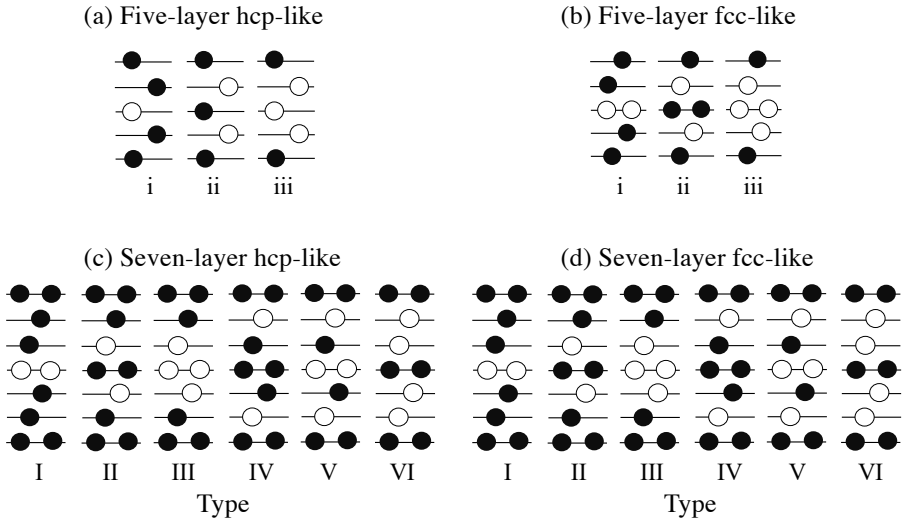

Fig. 3.1 Model of calculation. Possible atomic-layer alignments (a,b) in type i, ii, and iii structures for the five-layer and (c, d) in type I-VI structures for the seven-layer Co-based transition-metal thin films, for hcp-like and fcc-like stacking respectively. Where solid atoms are Co and open-circles represent other 3d elements (Ni, Fe, and Mn).

3.4 Bulk Co and pure Co thin films

3.4.1 MAE calculation

The MAE value is defined as the eigenvalue-sum difference between $[10\bar{1}0]$ and $[0001]$ magnetization direction, $E_{\mathrm{MA}} = E_{[10\bar{1}0]} - E_{[0001]}$. Positive value of MAE means that the favor magnetization direction is out-of-plane. Inversely, negative value of MAE means that in-plane magnetization direction is preferred. The total energy difference between hcp-like and fcc-like stacking $\Delta E = E_{\mathrm{tot}}^{\mathrm{hcp}} - E_{\mathrm{tot}}^{\mathrm{fcc}}$ is estimated for the stacking stability. I performed a **k**-point convergence test for MAE for bulk Co and Co_5-hcp thin film (see Fig. 3.2). To suppress numerical fluctuations, the need of 18816 ($28 \times 28 \times 22$) number of k-points for bulk Co and 5184 ($72 \times 72 \times 1$) for Co-based slab calculation were confirmed. The MAE converges to 0.04 meV/Co for bulk and 1.03 meV/unit-area for Co_5 hcp film.

Firstly, I carried out calculations of the magnetic properties of bulk hcp Co for comparison with those of Co thin film. DFT calculation was performed with the c/a lattice-constant ratio 1.63 [44]. The local spin magnetic moment and MAE of bulk Co are calculated as 1.75 μ_{B} and 0.04 meV/Co, respectively. The MAE value shows fair agreement with the experimental value, 0.07 meV/Co [46]. A theoretical work [44] has reported the value of 0.03 meV/Co (for $l_z = 2$) and -0.02 meV/Co (for $l_z = 3$) by means of the linear muffin-tin orbital method.

Table 3.1 shows the calculated MAE and total energy difference of pure Co films. The calculated MAE are 1.03 and 2.55 meV/unit-area (-0.07 and -0.68 meV/unit-area) for five- and seven-slabs, respectively, with hcp-like (fcc-like) stacking, manifesting that the easy magnetization direction is out-of-plane (in-plane). The positive, i.e. perpendicular, MAE values in the hcp stacking are remarkably larger than the MAE at bulk Co, which is calculated as 0.04 meV/Co. By comparing the total energy between the hcp and fcc stacking, fcc stacking is more stable by 0.19 eV/Co in the five-layer and hcp stacking is more stable by 0.01 eV/Co in the seven-layered film. This indicates that the thinner Co film favours fcc stacking with in-plane magnetization and the thicker film prefers hcp stacking with perpendicular magnetization, as the latter is consistent with the experimental measurement in bulk Co. When one fabricates thin films as varying their thickness, it may be possible to tune the magnetic direction by invoking a hcp-fcc phase transition [47, 48].

The spin magnetic moments of the constituent atoms in Co films are independent of the magnetization direction. The calculated results of spin magnetic moments for each kind of atom in Co films are presented in Table 3.2. Co1 is presented as the center layer atom, Co3 and Co4 are presented as surface layer atoms for five- and seven-layer slabs cases respectively. It is well recognized that the magnetic moment enhancement at the surface comes from the reduced number of nearest neighbors and hence weaker inter-atomic hybridization [49].

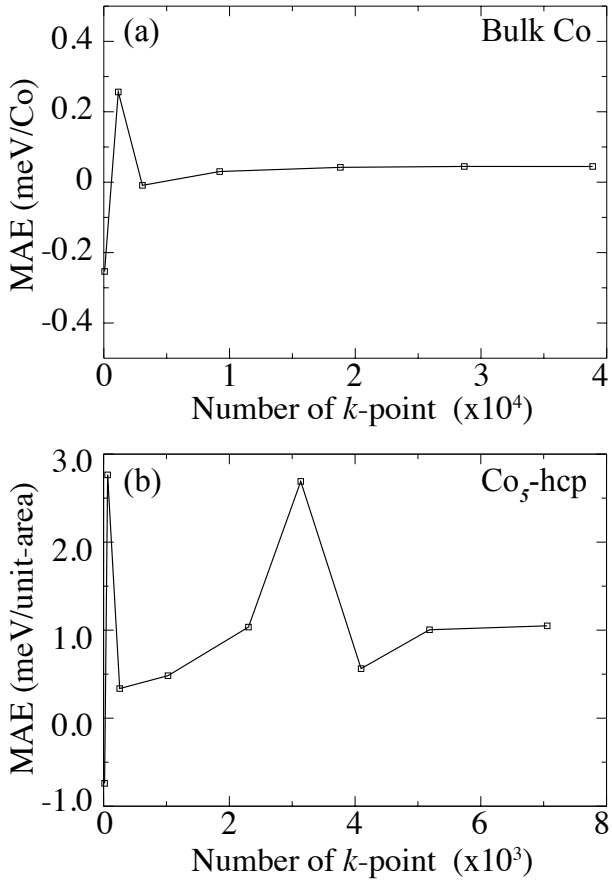

Fig. 3.2 **k**-dependence of MAE calculated in (a) bulk Co and (b) Co_5 hcp stacking thin film.

Table 3.1 Calculated MAE values (meV/unit area) and total energy differences (eV/f.u) of pure Co five- and seven-layer films for hcp and fcc stacking

Stacking	Five-layer slab		Seven-layer slab	
	E_{MA}	ΔE	E_{MA}	ΔE
Hcp(0001)	1.03	0.19	2.55	−0.01
Fcc(111)	-0.07	0	−0.68	0

Table 3.2 The spin contribution to the magnetic moment (in μ_B) for hcp and fcc in five- and seven-layer pure Co films.

Atomic layer	Five-layer slab		Seven-layer slab	
	hcp	fcc	hcp	fcc
Co1	1.76	1.83	2.78	1.87
Co2	1.81	1.91	1.77	1.84
Co3	1.86	1.90	1.82	1.90
Co4	-	-	1.87	1.90

Table 3.3 Orbital magnetic moments (in μ_B) depend on the magnetization direction and the anisotropy of the orbital magnetic moments for hcp and fcc in five- and seven-layer Co films.

	Five-layer slab		Seven-layer slab	
	hcp	fcc	hcp	fcc
$m_{\mathrm{orb}}^{[0001]}$	0.54	0.45	0.80	0.62
$m_{\mathrm{orb}}^{[10\bar{1}0]}$	0.46	0.44	0.62	0.62
Δm_{orb}	0.09	0.01	0.18	0.00

On the other hand, the orbital magnetic moments of Co films show a characteristic dependence on the magnetization direction. The anisotropy of the orbital magnetic moment defined by $\Delta m_{\mathrm{orb}} = m_{\mathrm{orb}}^{[10\bar{1}0]} - m_{\mathrm{orb}}^{[0001]}$ take the large positive value for hcp stacking, whereas it is nearly zero for fcc stacking.

3.4.2 Density of states

The magnetocrystalline anisotropy is determined by the characteristic of the band structure near the Fermi level in the systems concerned. Therefore, it would be interesting to examine the density of state (DOS) and energy bands of the systems in the vicinity of the Fermi level. Fig. 3.3 show the total DOS of five-layer slabs Co thin films for hcp and fcc stacking, and bulk Co respectively. In five-layer slab, the majority spin sate is almost fully occupied and is located from 1.0 to 5.0 eV below Fermi level. On the other hand, the minority spin states are partially occupied, resulting in a large DOS at the Fermi level. In these thin films, sharp peaks of the DOS can be found near the Fermi level in the minority spin state. The complicated peak structure around the Fermi energy is not present in a bulk Co (see Fig. 3.3) and originating from Co ions located near the surfaces in the slab. This lead to an enhancement of the MAE in slab structure compared from tiny MAE in bulk Co.

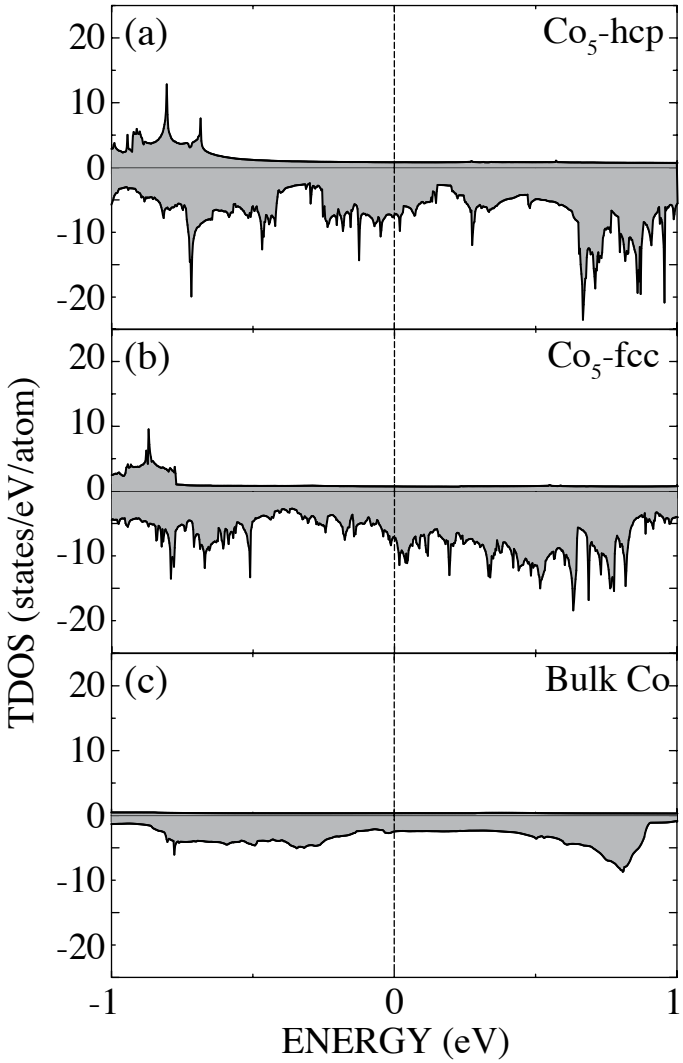

Fig. 3.3 DOS of pure Co five-layer thin film with (a) fcc and (b) hcp-stacking, and DOS of (c) bulk Co. A vertical dashed line denotes the Fermi energy.

3.5 Co-based thin films

3.5.1 Dependence of magnetocrystalline energy on layer stacking

Next, let us look at the calculated MAE at the Co-based transition-metal thin films with five-layered slabs summarized in Fig. 3.4(a). Interestingly, the Ni-Co system shows the perpendicular MAE for both hcp- and fcc-stacking with all the three stacking patters considered here. The largest positive values of MAE, $E_{\mathrm{MA}} = 1.52$ and 1.39 meV/unit-area, are observed at type iii of Ni-Co thin film, Co-Ni_3-Co, for fcc and hcp stacking, respectively. It is even remarkable that the MAE values exceed that of pure cobalt slab while the other slabs show lower and/or negative MAE values. The characteristic of this slab is that Ni atoms are located at the inner three layers of the slab and Co atom is placed at the outmost surfaces. This same goes for the seven-layered slabs: in the Ni-Co slab that contains many Ni atoms at inner layers (such as type III, V, and VI) show large perpendicular MAE although they don't exceed MAE of the pure cobalt. Fe-Co and Mn-Co systems mostly show negative (in-plane) MAE. It should be noted that the perpendicular MAE in Ni-Co system has been proposed by Daalderop *et al.*; their computational and experimental work indicates that tuning of thickness of Co/Ni multilayer leads to a perpendicular orientation of the magnetization while their simulation was based on a different model from the present work [50]. In the following subsection, I will discuss the mechanism of how the Ni-Co stacking enhances the perpendicular MAE.

3.5.2 Microscopic mechanism of magnetocrystalline anisotropy

In order to understand the microscopic mechanism of MAE, I evaluated the E_{MA} contribution on the k space, according to the following equation,

$$\begin{aligned} E^{k}_{\mathrm{MA}} &= \sum_{m} \left(\varepsilon^{10\bar{1}0}_{m\mathbf{k}} - \varepsilon^{10\bar{1}0}_{\mathrm{F}} \right) - \sum_{n} \left(\varepsilon^{0001}_{n\mathbf{k}} - \varepsilon^{0001}_{\mathrm{F}} \right) + \Delta E_{\mathrm{F}}, \\ \Delta E_{\mathrm{F}} &= N_{\mathrm{e}} \left(\varepsilon^{10\bar{1}0}_{\mathrm{F}} - \varepsilon^{0001}_{\mathrm{F}} \right), \end{aligned} \tag{3.1}$$

where $\varepsilon^{10\bar{1}0}_{m\mathbf{k}}$ and $\varepsilon^{0001}_{m\mathbf{k}}$ represent the energy of band m when the magnetization is set parallel to the $[10\bar{1}0]$ axis and the [0001] axis, respectively. It should be noted that the Fermi energy changes slightly when the magnetization is directed from the in-plane to the perpendicular direction. If one simply subtracts the band energy with the perpendicular axis from that with the in-plane axis, the excessive difference appears due to the difference in the number of bands. To fix this problem, I added a term of ΔE_{F} (change of Fermi energy) into the equation.

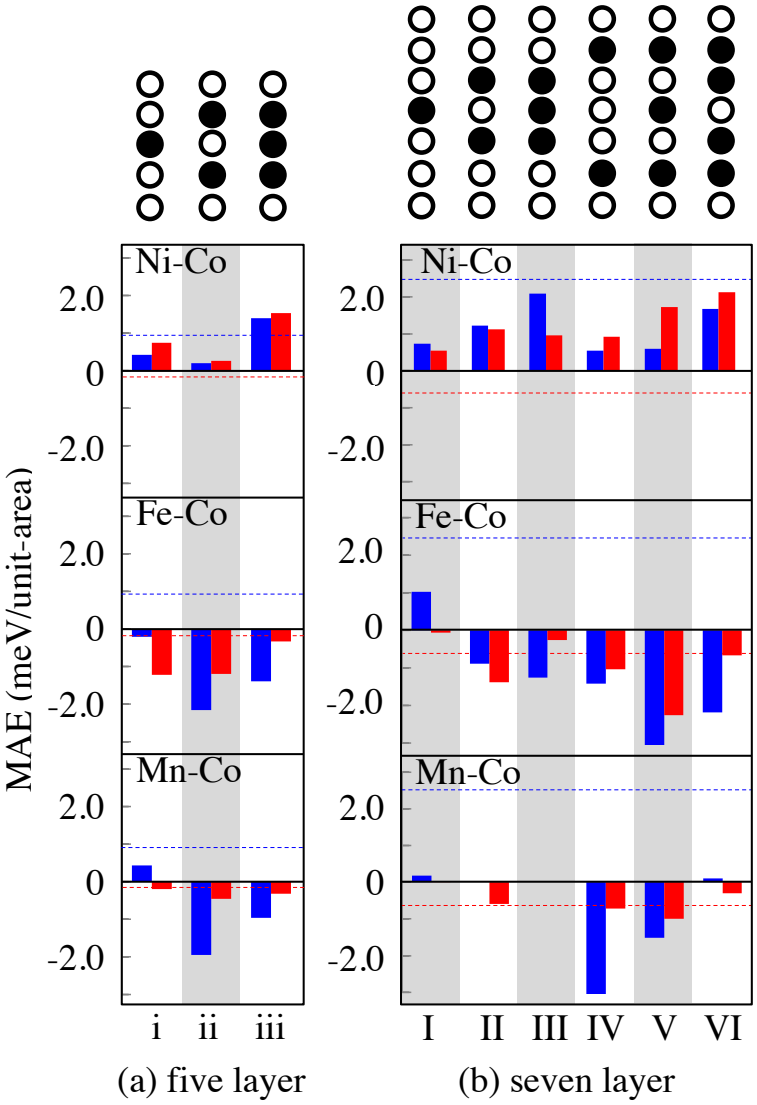

Fig. 3.4 Top: Schematic stacking patterns of TM-Co slabs. Open and closed circles indicate Co and TM atoms, respectively. Bottom: Calculated MAE for Ni-Co, Fe-Co, Mn-Co multilayers for each stacking pattern in (a) five-layered slabs and (b) seven-layered slabs. Blue bar is for hcp-like and red bar is for fcc-like structure. Positive values correspond to perpendicular-favored anisotropy. Horizontal dashed lines with blue and red colors indicate MAE for pure Co films with hcp and fcc stacking structures for reference.

Fig. 3.5 shows the *d*-orbital projected bandstructure with the MAE contribution in the *k* space for Co_5 hcp thin film. It shows negative MAE around the K point, while there is no pair of unoccupied and occupied bands that can contribute to MAE. At the Γ point, both the unoccupied and occupied bands near the Fermi energy consist of $3z^2 - r^2$ orbital state at Co1-3 sites, such m=0 orbital states being not supposed to contribute to MAE.

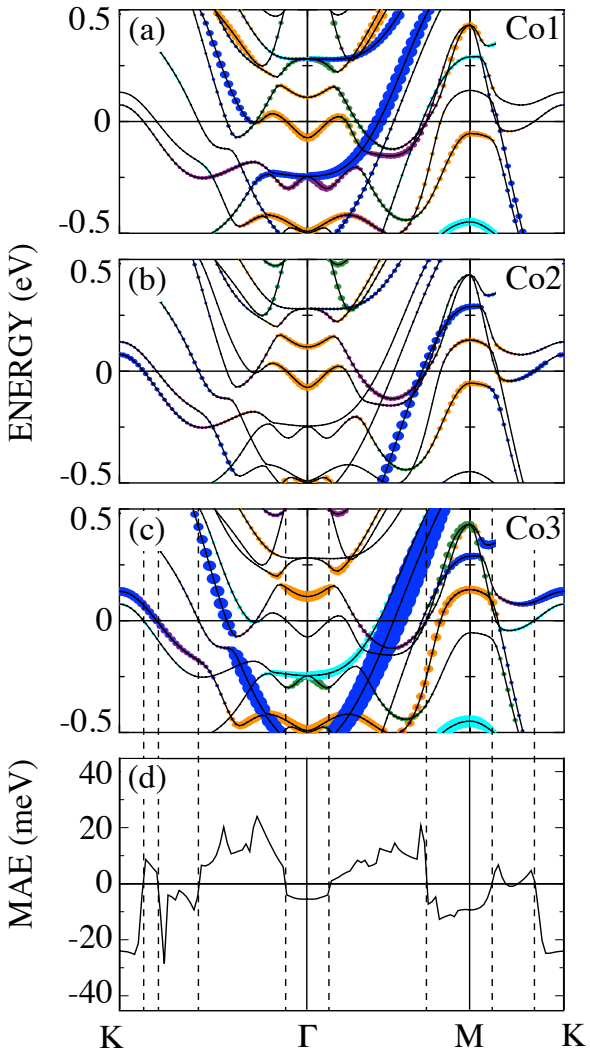

Fig. 3.5 Minority-spin band structure (a)-(c) for Co_5 thin films with hcp-like stacking The color highlighting the bands represent *d*-orbital components as follows; orange: $3z^2 - r^2$, green: xz, cyan: yz, purple: $x^2 - y^2$, and blue: xy for each kind of atoms. (d) present the calculated MAE contribution in *k* space.

Fig. 3.6 shows the calculated MAE contribution in the *k* space, E^k_{MA}, for Co-Ni_3-Co (type iii) slabs with hcp-like structures. By comparing Fig. 3.6 (c) and (d), one can observe

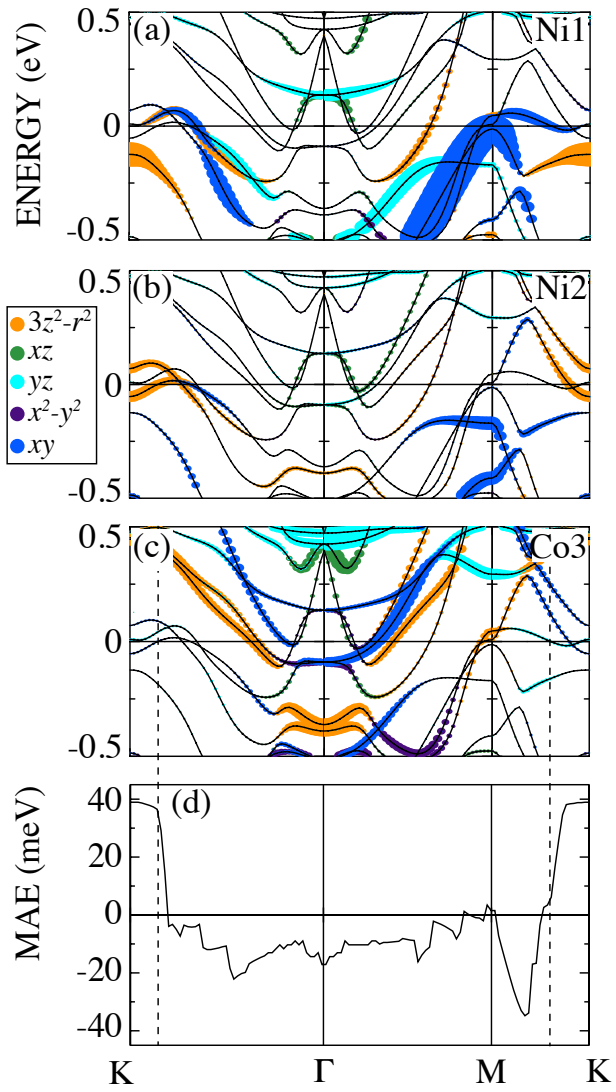

Fig. 3.6 (a)-(c) Minority-spin band structure for Co-Ni_3-Co (type iii) in five-layered thin films with hcp-like stacking. Due to the mirror symmetry, in the five-layered slab, the surface layer is denoted as Co3, sub-layer is Ni2 and center layer is Ni1. The color highlighting the bands represent d-orbital components as follows; orange: $3z^2 - r^2$, green: xz, cyan: yz, purple: $x^2 - y^2$, and blue: xy for each kind of atoms. (d) The calculated MAE contribution in k space. Vertical dashed lines point the locations where the MAE changed the value significantly and the link with the corresponding band crossing the Fermi energy.

that E^k_{MA} changes its value significantly when one of the bands crosses the Fermi energy. For instance, a band with a large weight of Ni2:$3z^2 - r^2$ character is responsible for a change of MAE at the KΓ line and one with Ni1:xy character is responsible for a change at the MK line. This behavior can be understood by considering the SOC effect as a perturbation to the band structure.

According to the second-order perturbation theory of SOC proposed by Bruno [29], there is a strong connection between MAE and the orbital moment. The change in the total energy by SOC comes from the interaction between occupied and unoccupied states. This gives

$$\begin{aligned} E_{\mathrm{SOC}} &= -\sum_{o,u} \frac{\left|\langle o|\sum_i H^{(i)}_{\mathrm{SOC}}|u\rangle\right|^2}{\varepsilon_u - \varepsilon_o} \\ &= -\sum_{o,u} \frac{\left|\langle o|\sum_i \xi^{(i)}\mathbf{L}^{(i)}\cdot\mathbf{S}^{(i)}|u\rangle\right|^2}{\varepsilon_u - \varepsilon_o}, \end{aligned} \tag{3.2}$$

where $H^{(i)}_{\mathrm{SOC}}$, $\xi^{(i)}$, $\mathbf{L}^{(\mathbf{i})}$, $\mathbf{S}^{(\mathbf{i})}$ represent the on-site SOC term, the coupling constant of the spin-orbit interaction, orbital and spin momentum operator at atom i, respectively; o (u) and ε_o (ε_u) represent occupied (unoccupied) eigenstates and those eigenvalues. MAE is the difference between the SOC energies for two magnetization directions (e.g. **x** and **z**),

$$E_{\mathrm{MA}} = E_{\mathrm{SOC}}(\mathbf{x}) - \mathbf{E}_{\mathrm{SOC}}(\mathbf{z}). \tag{3.3}$$

Here I consider that the majority (↑) spin state is fully occupied and not responsible for the MAE while the minority (↓) spin states is partially occupied and considered to determine MAE for late transition-metal elements. When the effect of the majority spin states and the interaction between majority and minority spin states are neglected, only the SOC interaction between minority-spin states (↓↓) have to be considered. Since the matrix element $\langle o^{\downarrow}|\mathbf{L}\cdot\mathbf{S}|\mathbf{u}^{\downarrow}\rangle$ is equal to $\langle o^{\downarrow}|\frac{1}{2}L_\zeta|u^{\downarrow}\rangle$, where L_ζ is the expectation value of the **L** component parallel to the spin quantization direction, I obtain

$$E^{\downarrow\downarrow}_{\mathrm{MA}} = \frac{1}{4}\sum_{o,u} \frac{|\langle o|\sum_i \xi^{(i)}L^{(i)}_z|u\rangle|^2 - |\langle o|\sum_i \xi^{(i)}L^{(i)}_x|u\rangle|^2}{\varepsilon_u - \varepsilon_o}. \tag{3.4}$$

It leads to the fact that the SOC between occupied and unoccupied states with the same and non-zero (different by one) m magnetic quantum number makes a positive (negative) contribution to the MAE through L_z (L_x) operator. This can indeed explain the MAE in a free-standing Fe monolayer [29, 51].

However, Bruno's theory fails to explain the k-dependency of MAE in the Co-Ni_3-Co case. Although E^k_{MA} shows the maximum value around the K point, both the unoccupied and occupied bands near the Fermi energy mainly consist of Ni2:$3z^2 - r^2$ orbital state (see Fig. 3.6 (a)-(c)), such m=0 orbital states being not supposed to contribute to MAE through Eq. 3.2. Around the Γ point, Ifind that the unoccupied and occupied bands consist of Co3:xy (m=±2) orbital states near the Fermi energy. The SOC is expected for positive contribution to MAE but the calculated E^k_{MA} is negative there.

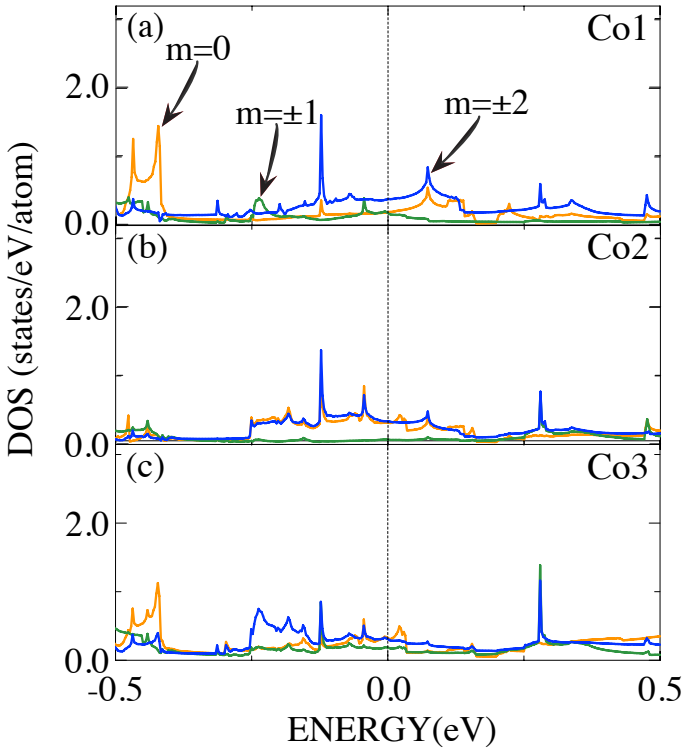

Fig. 3.7 The partial density of state of minority spin state in small range energy around E_F for each atomic layer in Co_5 hcp film. The color represent d orbital state as follows; orange: m=0, green: m=±1, blue: m=±2.

The partial DOS of each atomic layer is shown in Fig. 3.7 for Co_5 hcp films which specify different d orbital state for each atomic layer. As being different from Co-Ni_3-Co (type iii) case, small density of state around Fermi energy leads to a negative single-layer contributions in Co_5, while the positive inter-layer contributions originate from the strong hybridization between different Co layers through the peak of m=±2 orbital state located near the Fermi energy. The density of state at the surface Co (Co3) layer is also different between Co-Ni_3-Co and Co_5 cases, resulting in those different contributions to MAE.

Table 3.4 Orbital magnetic moments (μ_B) with out-of-plane [0001] and in-plane $[10\bar{1}0]$ magnetization directions, intra-layer contributed MAE (meV/unit-area)for each atomic layer in Co-Ni_3-Co and Co_5 films with hcp stacking.

Co-Ni_3-Co	Ni1	Ni2	Co3
$m_{\mathrm{orb}\_}^{[0001]}$	0.07	0.07	0.13
$m_{\mathrm{orb}}^{[10\bar{1}0]}$	0.04	0.06	0.12
E_{MA}	0.93	0.20	0.45
Co_5	Co1	Co2	Co3
$m_{\mathrm{orb}\_}^{[0001]}$	0.11	0.10	0.12
$m_{\mathrm{orb}}^{[10\bar{1}0]}$	0.08	0.07	0.12
E_{MA}	0.04	-0.46	-0.06

Table 3.4 shows the orbital moments and MAE contribution for each atomic layer in Co-Ni_3-Co and Co_5 films. Orbital moment of in-plane magnetization direction $[10\bar{1}0]$ is smaller than out-of-plane direction [0001] in each atomic layer of both films, while the calculated MAE contribution shows positive values for Ni1, Ni2, and Co3 in Co-Ni_3-Co film and negative values for Co2 and Co3 in Co_5 film. The same behavior was checked for other materials in this study; *i.e.,* no connection between MAE and the orbital moment was found. Here, I evaluated the single-atomic-layer contribution to MAE by taking the difference between fully-SOC calculated MAE (as switching on SOC at all the atoms) and the SOC-off MAE (as switching off SOC at one atomic layer). Note that it is considered as single-atomic-layer contribution instead of a single-atom contribution since the atoms are periodically aligned in the *xy* plane and the inter-site terms between the same-layer atoms are contained in the contribution. It turns out that Ni1 atomic layer dominantly contributes to positive MAE in Co-Ni_3-Co layer. Although such a positive contribution from Ni1 is not detected in the band structure in Fig. 3.6 (a) and (d), the partial density of state (shown in Fig. 3.8) gives a clue to explain it. At Ni1 layer, $m = \pm 2$ state, which is likely spreading over general *k*-points, shows large weight at Fermi energy. Its contribution to MAE is expected to be positive by Bruno's theory.

Fig. 3.9 shows the contribution from each atomic layer in Co-Ni_3-Co and Co_5 films with hcp-like stacking. It is seen that the summation of the atomic-layer contribution (1, 2, 3) does not match the fully-SOC calculated MAE (F). This is because the full MAE is not composed

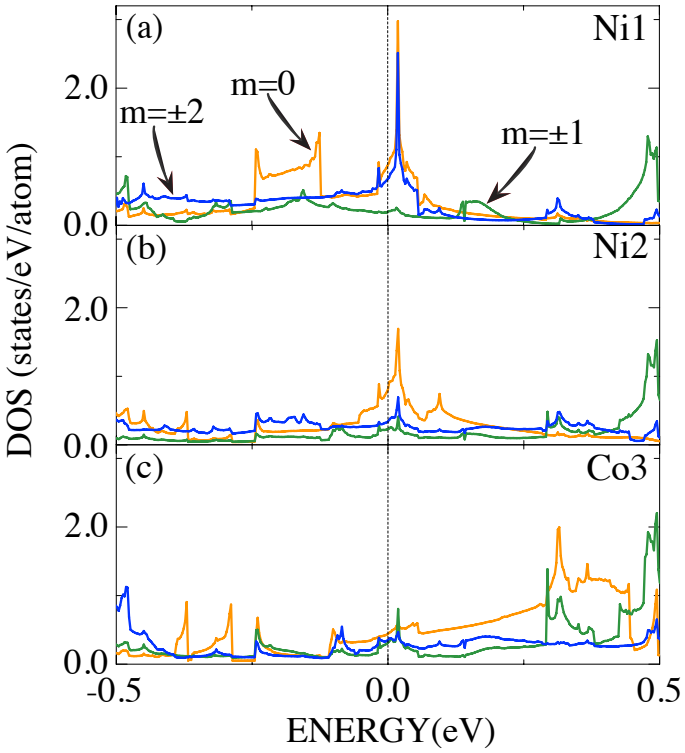

Fig. 3.8 The partial density of state of minority spin state in small range energy around E_F for each atomic layer in Co-Ni_3-Co (type iii). The line color represents *d* orbital characters as follows; orange: m=0, green: m=±1, blue: m=±2.

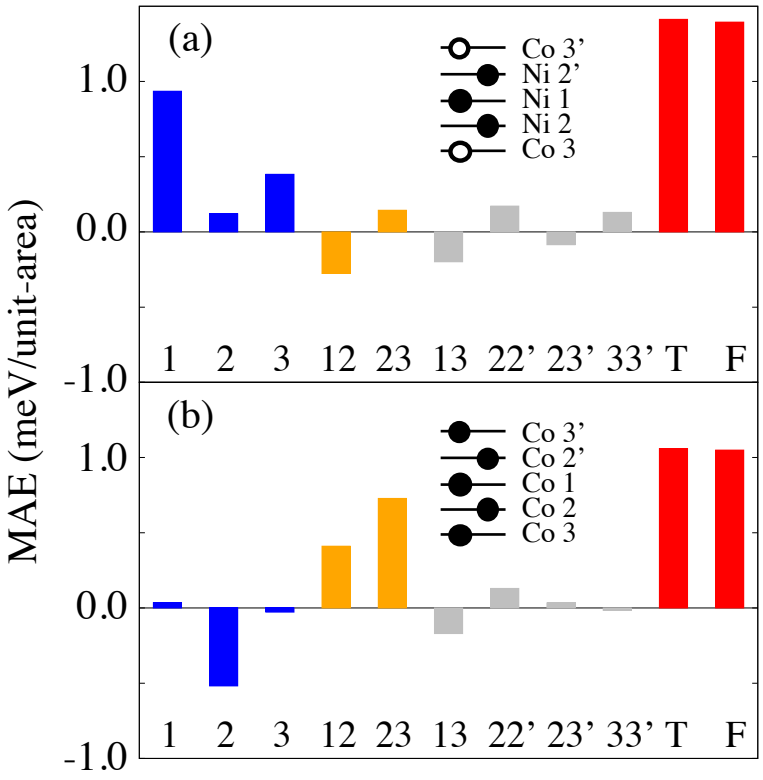

Fig. 3.9 (a) MAE contribution of each atomic layer (blue bar; the contributions from the symmetrically equivalent layers, 2 and 2'; 3 and 3', are summed up); first nearest inter-layer (yellow bar); second and third nearest inter-layer (grey bar); total (summation of all the contributions) and fully-SOC calculated MAE (red bar) in Co-Ni_3-Co (type iii) multilayers (a) and Co_5 (b) with hcp-like stacking. Atomic number is labeled as shown in insets. Due to the mirror symmetry, there are two equivalent atomic sites except for the middle one.

only of the summation of single atomic-layer contributions but also of other contributions:

$$E_{\mathrm{MA}} = E_{\mathrm{SOC}}(\mathbf{x}) - \mathbf{E}_{\mathrm{SOC}}(\mathbf{z}) + \mathbf{E}'_{\mathrm{SOC}}(\mathbf{x}) - \mathbf{E}'_{\mathrm{SOC}}(\mathbf{z}), \tag{3.5}$$

$$E'_{\mathrm{SOC}} = -\sum_{i\neq j}\sum_{o,u} \frac{\left\langle o|H^{(i)}_{\mathrm{SOC}}|u\right\rangle \left\langle u|H^{(j)}_{\mathrm{SOC}}|o\right\rangle}{\varepsilon_u - \varepsilon_o}, \tag{3.6}$$

where E_{SOC} is same as Eq. 3.2 and E'_{SOC} is a newly introduced inter-layer term[52]. When $3d$ orbital states between two neighboring layer atoms (i and j) are strongly hybridizing and forming both occupied and unoccupied states ($|o\rangle$ and $|u\rangle$), the inter-layer term ij can effectively contribute to the MAE. Since the $|o\rangle$ and $|u\rangle$ states are described as mixed orbital states with complex coefficients, the second term is difficult to be further simplified unlike the first term. Ihere computationally evaluated the inter-layer contribution by taking the difference between the MAE as switching off SOC at two atomic layer and the summation of two individual single-atomic layer contributions.

In Co-Ni_3-Co film (see Fig. 3.9(a)), the positive MAE is mainly contributed from the single atomic-layer SOC at Ni1, while the inter-layer terms, such as Ni1-Ni2 and Ni1-Co3, negatively contribute to the total MAE. In Co_5 film (see Fig. 3.9(b)), surprisingly, the inter-layer terms, Co1-Co2 and Co2-Co3 contribute to MAE dominantly with the positive sign while the single-layer terms at Co2 contributes less with the negative sign. The enhancement of the inter-layer terms originates from the stronger hybridization between Co and Co atoms than that between Co and Ni atoms. In both cases, a summation of all the single-atomic layer contributions and all the nearest inter-layer contributions shows a successful agreement with the full SOC calculated MAE (compare T and F in Fig. 3.9). The impact of inter-site SOC term on MAE makes a striking contrast to previous works on FePt, Au/Co/Au, and $CrNb_3S_6$, where the on-site term and inter-atomic term with $3d$-$5d$ or $3d$-$4d$ hybridization collaborate to enhance the net MAE [52–54]. As I come back to the band structure of Co-Ni_3-Co shown in Fig. 3.6, E^k_{MA} shows large positive value around the K point, where the occupied and unoccupied bands near the Fermi energy consist of Ni2:$3z^2 - r^2$ orbital states. As discussed above, the on-site SOC term doesn't contribute to MAE with such $m = 0$ state, while the inter-layer term between Ni2 and Ni2' atoms may positively contribute to MAE as being consistent with the positive contribution of 22' shown in Fig. 3.9(a). Similarly, the negative MAE around the Γ point can be explained by Ni1-Co3 inter-layer term. This result manifests the importance of cross coupling between the inter-layer hybridization and the SOC in $3d$ transition-metal thin films.

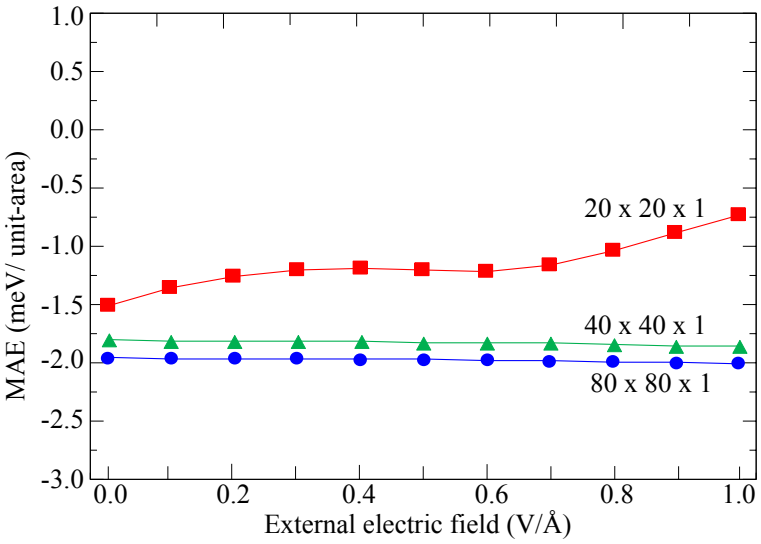

Fig. 3.10 **k**-dependence of calculated MAE as a function of the external electric field for free-standing Co monolayer. The color represent the different *k*-mesh as follows; red: 20 × 20 × 1, green: 40 × 40 ×1, blue: 80 × 80 × 1.

3.6 Electric field effect on magnetocrystalline anisotropy

Finally, I discuss the effect of electric field on the MAE in Co-based thin film. The modification of magnetic moments and MAE in ultrathin cobalt films by external electric field has been experimentally reported by Kawabe *et al.* [38]. In monolayer Co, I investigate the MAE as a function of the external electric field with different *k*-mesh, as shown in Fig. 3.10. The electric field, however, does not give any effect on the MAE with the fine *k*-mesh (80 × 80 × 1). Ref. [55] has shown that external electric field only can modify the MAE a Fe(001) monolayer but not in Co(001) monolayer.

Electric fields were applied perpendicular to the film slab. Fig. 3.11 and 3.12 show the saw-like potential with the distance of model with applied electric field is zero and 0.2 V/Å in Co_5 thin film, respectively. The dipole correction is also added into the calculation including the external electric field, which is the correction in the vacuum area shown in Fig. 3.12. In metallic systems like Co-based thin film, the electric field has a large screening effect. Due to this effect, we can expect a small effect of the electric field in the MAE.

Fig. 3.13 shows the calculated MAE as a function of the electric field of Co_5 and Co-Ni_3-Co in hcp stacking. In pure Co film, as I predict for monolayer, the electric field does not have any effect on the MAE. On the other hand, the MAE of Co-Ni_3-Co is modified by 0.1 meV/ unit-area with applied electric field 0.8 V/Å. The MAE in Ni-Co film can be controlled by the electric field through a change of the charge around the Fermi level. The DOS of Co-Ni_3-Co film with and without external electric field are given in Fig. 3.14. In

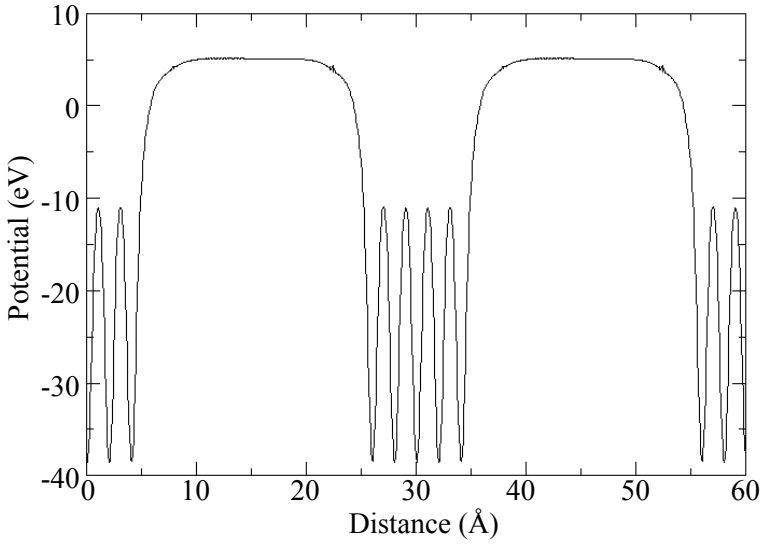

Fig. 3.11 Saw-like potential in Co_5 film in zero external field.

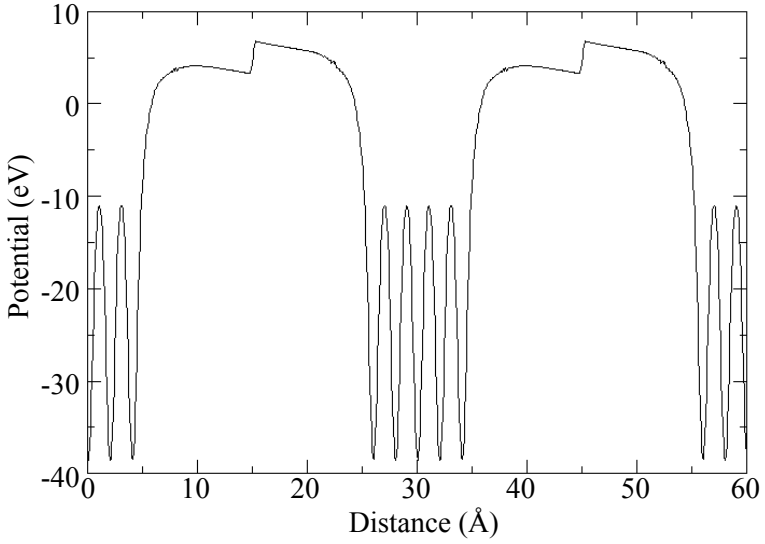

Fig. 3.12 Saw-like potential with dipole correction at the vacuum in Co_5 film in the applied external field 0.2 V/Å.

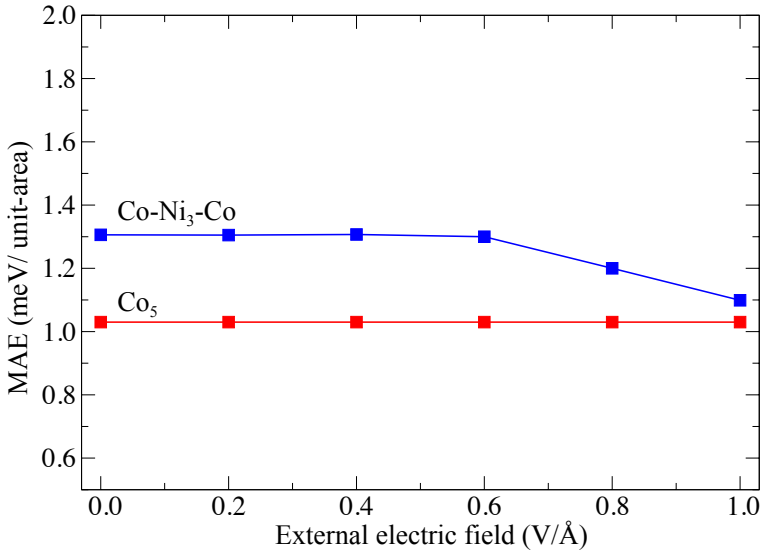

Fig. 3.13 Calculated MAE as a function of the external electric field for (blue curve) Co_5 and (red curve) Co-Ni_3-Co with hcp stacking.

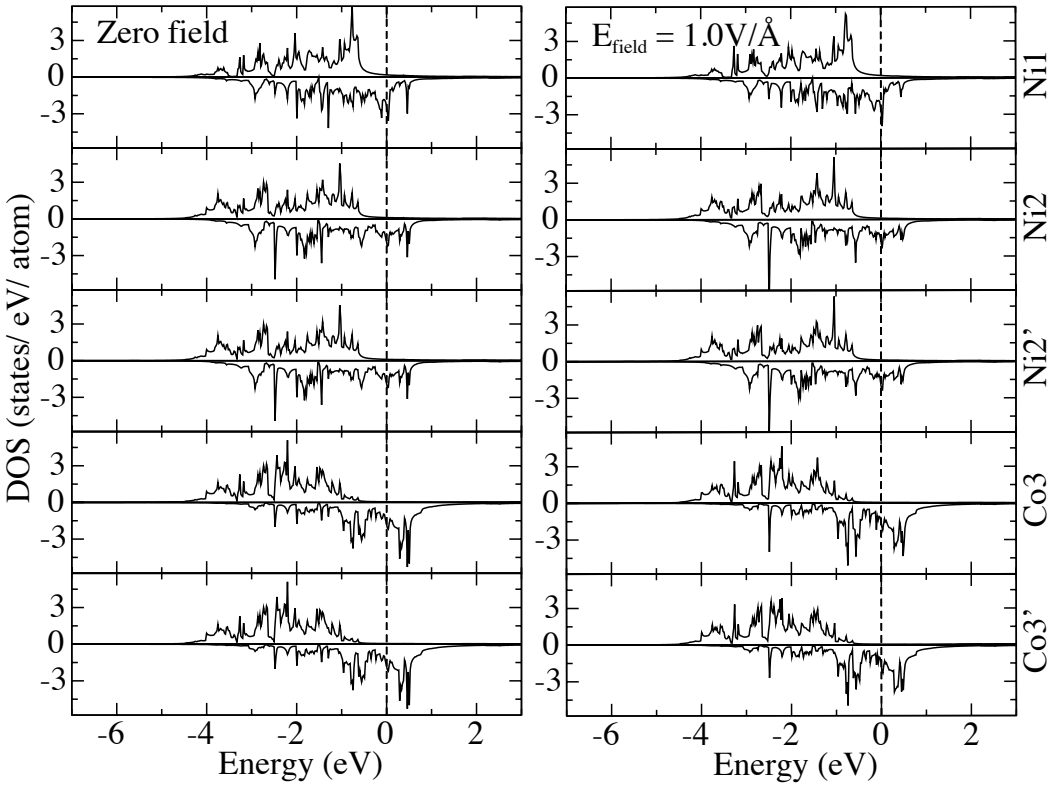

Fig. 3.14 *d*-orbitals projected DOS in the muffin-tin spheres of Co-Ni_3-Co with hcp stacking in an external electric field of (a) zero and (b) 1.0 V/Å for each atomic layers. A vertical dashed line denotes the Fermi energy.

minority spin, at the energy range -1.0 eV < E_F < 1.0 eV, the modification of the occupied and unoccupied states around the Fermi level lead to the modification of the MAE. In the inner three Ni-layers, the DOS peak remains at the Fermi level. The modification by electric field can be found at two surface Co-layers, where DOS peaks below and above Fermi has changed the amplitude. The charge at surfaces compensated by surface dipole plays a role when introducing external electric fields.

Chapter 4

Electric field effect on magnetic stability in 2D magnetic materials

4.1 Introduction

Two-dimensional (2D) van der Waals (vdW) materials with the intrinsic magnetism have received extensive interest from the experiment achievement in atomic-layers CrI_3, $Cr_2Ge_2Te_6$ and Fe_3GeTe_2 [56–58]. Interestingly, the thickness of one or a few atomic layers enable the control of 2D magnetism by means of external electric field [59–61], electron-hole doping [58, 62] appealing to their potentials for future spintronics applications.

Two-dimensional honeycomb structure ferromagnet CrI_3, which belongs to a family of transition-metal trihalides MX_3 with X = Cl, B, and I [56, 59–68] is considered as a promising candidate material for future spintronics applications. Very recently, VI_3 has emerged as a newly discovered 2D material that belongs to the transition-metal trihalides [69–75]. It has been known for more than 30 years that in the bulk form, VI_3 becomes ferromagnetic (FM) below the Curie temperature, T_c=55K as against T_c=68K for CrI_3 [76]. Recent experimental studies have reported that VI_3 exhibits a structural phase transition that changes its symmetry at 79K [69, 70], while the crystal structure in either phase has not been uniquely resolved yet. The high-temperature (HT) crystal structure was proposed as trigonal $P31c$ [69], rhombohedral $R3$ [75], and monoclinic $C2/m$ structure [70]. The low-temperature (LT) crystal structure was proposed as $C2/c$ [69] and $R\bar{3}$ structure [70].

Optical and electrical transport measurements have showed bulk VI_3 to be an insulator with an optical band gap of 0.67 eV [69]. However, from the theoretical point of view, the understanding and modeling of the electronic properties are the center of current studies. Some theoretical studies have in fact reported that bulk VI_3 is a Mott-insulator with a band

gap of about 1.0 eV [69, 70], whereas other studies have claimed that bulk VI_3 shows half-metallic state [74, 75].

In the thin film limit, to the best of our knowledge, no experimental studies have been reported for the atomic layer of VI_3. On the other hand, DFT studies are rather controversial about the ground state of V-3d^2 state in bilayer VI_3. Ref. [71] has proposed the Mott-insulator ground state which has a lower total energy ($\sim$0.3 eV/f.u) than the half-metallic state. Ref. [72] has proposed orbital-ordered phases that accompany the lattice distortion. Ref. [73] has proposed a fully orbital-moment polarized state which is stabilized by combination of spin-orbit coupling and Hubbard U.

In bilayer VI_3, the inter-layer magnetic stability has been theoretically studied. Ref. [71] has reported that inter-layer magnetic stability is sensitive to the layer stacking, as being consistent with previous works on bilayer CrI_3 [64–66]. Ref. [77] has claimed that bilayer VI_3 shows stacking-independent FM ground state while they have considered the half-metallic state instead of Mott insulating state.

In this study, I study the electronic structures and magnetic properties of VI_3 in comparison with CrI_3 by DFT approach and give a focus to the role of the partially filled t_{2g}^2 orbital state in VI_3. The electric field control of magnetic stability in bilayer VI_3 will be investigated. The microscopic understanding of electric-field induced magnetic stability will be studied via the virtual hopping mechanism.

4.2 Computational methods

Density-functional theory (DFT) calculations were performed using the VASP code [78] within the generalized gradient approximation (GGA) [9]. The vdW interactions were included for bilayer structure calculations. The rotationally invariant GGA + U method was employed to account for correlation effects [79]. On-site Coulomb interaction for V-3d orbital was considered with an effective U value of 2.0 eV [60]. Brillouin zone integrations were performed using a k-point grid of 6 $\times$ 6$\times$ 1 to relax the structures. Band structures and DOS, including electric field, were plotted by using 12 $\times$ 12 $\times$ 1 k-point mesh. The electric field is applied perpendicular to the surface by saw-tooth-like potential with dipole correction [14]. In order to perform the MLWFs, I use Wannier90 tool [80] together with the VASP code.

4.3 Model of Calculations

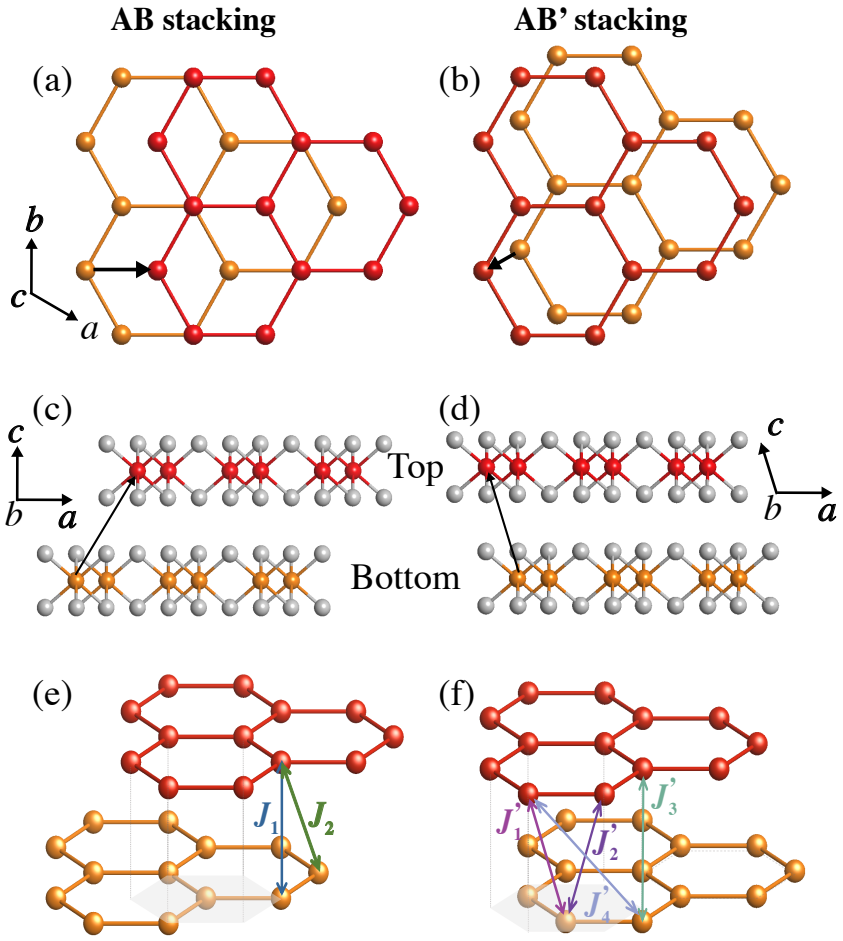

Fig. 4.1 (a, b) Top views and (c, d) side views of atomic structure in bilayer VI_3 in AB and AB′ stacking. The red and orange hexagons represent the honeycomb structure of V atoms in the top and bottom layers, and gray balls represent I atoms. The black arrow indicates the vector which connects equivalent atoms located in two layers and shows how the top layer is sliding with respect to the bottom layer. Inter-layer exchange coupling J_{ij} in bilayer VI_3 for (e) AB and (f) AB′ stacking.

I consider that bilayer VI_3 has a similar atomic structure to its bulk counterpart. In this study, I assumed two structures corresponding to $R\bar{3}$ and $C2/c$ phases in bulk VI_3 [70]. The difference between these two structures can be viewed as the different stacking orders of two single layers VI_3. As shown in Fig. 4.1 (a) and (c), the stacking order is similar to AB-stacked bilayer graphene, in which the top layer is displaced so that one V atom sits above a hexagon center of the bottom layer. By comparing the equivalent atoms between two layers, the top layer is horizontally shifted from the bottom layers by $(2\mathbf{a}+\mathbf{b})/\mathbf{3}$ (shown by a black arrow), where **a** and **b** are the lattice vectors. This structure has $R\bar{3}$ symmetry. As shown in Fig. 4.1 (b) and (d), the shift of top layer is $-(\mathbf{a}+\mathbf{b})/\mathbf{2}$ in AB$'$ stacking. The structure has $C2/m$ space-group symmetry. I employed the experimental values for the in-plane lattice constants in bulk VI_3: $a = b = 6.84$ Å [70]. The same initial structure models are prepared for bilayer CrI_3 with in-plane lattice constants $a = b = 6.866$ Å [63]. The 20 Å-thick vacuum is contained in the supercell for 2D slab calculation.

4.4 Results for monolayer VI_3

4.4.1 Crystal-field splitting

First I focus on the difference of crystal field effects in CrI_3 and VI_3 monolayers. In particular, both CrI_3 and VI_3 show the magnetic atom oordinated to six I atoms, forming edge-sharing octahedra and resulting in octahedral crystalline electric field (CEF) splitting of the d orbitals into the two-fold e_g and three-fold t_{2g} states. Nevertheless, the I-Cr-I bond angle in CrI_3 is almost 90° (*i.e.* a cubic octahedron), while the I-V-I angle in VI_3 approaches 89°. As such, it exhibits a trigonal distortion - elongation along the z axis - still preserving spatial inversion symmetry [see Fig. 4.2 (a) and (b)]. This Jahn-Teller (JT) distortion leads to a further splitting of t_{2g} levels into a doublet e_g' and a singlet a_{1g} [73, 81]. Fig. 4.2 (c) and (d) show the difference in CEF splitting for CrI_3 and VI_3 respectively: as schematically represented, the JT-induced splitting allows for the band gap opening in VI_3 by half-filling the majority e_g' channel and leaving the a_{1g} empty in the case of V d^2. On the other hand, CrI_3 is unaffected both because of the Cr d^3 valence and the almost cubic CEF.

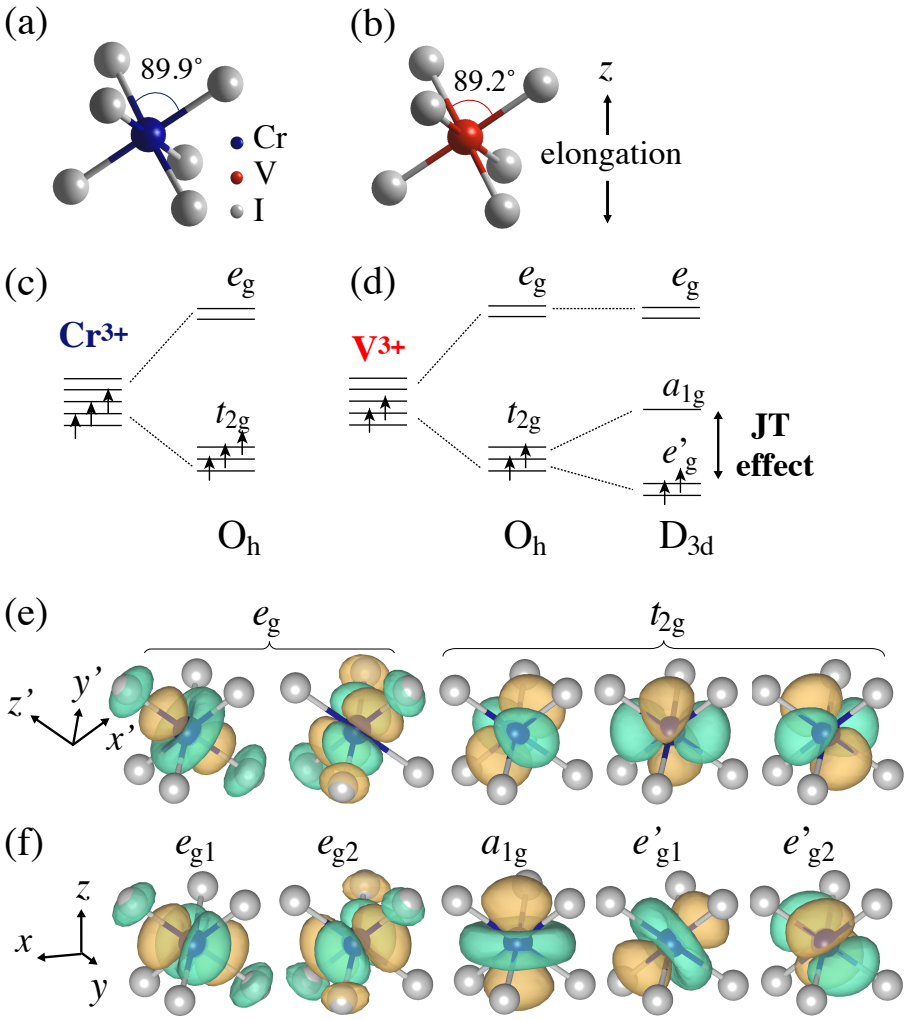

Fig. 4.2 Distortion of the crystal structure in (a) CrI_3 and (b) VI_3. The distortion does not change the bond length but alters the bond angle, leads to trigonal elongation along the z-direction. (c) and (d) show the crystal field splitting of d level in Cr $3d^3$ and V $3d^2$, respectively. Five $3d$ Wannier functions reflect the cubic CEF states in monolayer CrI_3 (e) and trigonal CEF states in monolayer VI_3 (f). The isosurface levels of the Wannier functions were set at $1.5\ a_0^{-3/2}$ (yellow) and $-1.5\ a_0^{-3/2}$ (blue), where a_0 is the Bohr radius.

Within the global Cartesian $\{xyz\}$ coordinate system, Fig. 4.2(f), the a_{1g} and e'_g states are written in the form [82]

$$\begin{aligned} |a_{1g}\rangle &= 3z^2 - r^2 \\ |e'_{g1}\rangle &= \frac{1}{\sqrt{3}}\left(\sqrt{2}\left(x^2 - y^2\right) - zx\right) \\ |e'_{g2}\rangle &= \frac{1}{\sqrt{3}}\left(\sqrt{2}xy + yz\right) \end{aligned} \tag{4.1}$$

where the z axis is parallel to the out-of-layer direction (*i.e.* perpendicular to the slab).

4.4.2 Wannier interpolation

According to the different local crystal field effects, I projected the Bloch functions onto the local MI_6 octahedral coordinate system $\{x'y'z'\}$ for CrI_3 (with basis axes directed along the Cr-I bonds), and onto the Cartesian $\{xyz\}$ system for VI_3.

I constructed the Wannier functions by projecting the specified set of Bloch states onto a set of 56 localized orbitals (i.e. 4×5 d orbitals and 12×3 p orbitals). These atomic orbital functions are carefully chosen so that the resulted MLWF represent the CEF orbitals. Projection for TM d orbitals for O_h CEF orbitals are set as

```
c = 0.0000, 0.0000, -3.2891: !TM site
dz2; dx2-y2; dxy; dxz; dyz: !all d orbitals
z = 0.81, 0.00, 0.58: !are rotated in
x = -0.41, 0.70, 0.58 !bond direction
```

in seedname.win file for Wannier90 code.

The d states were projected onto the cubic CEF orbital states of which the local z' and x' axes are set parallel to the TM-I bond axes (see Fig. 4.2(c)). I-p states are projected onto p_x, p_y, p_z states with the global Cartesian coordinate since the orbital shape of I-p WFs are automatically determined by the unitary transformation after the TM-d WF projection is set and the initial projection choice of p states doesn't change the result.

The d-orbital projection for D_{3d} CEF orbitals are set as

```
c = 0.0000, 0.0000, -3.3337:!TM site
dz2; dx2-y2:!eg orbitals
z = 0.81, 0.00, 0.58: !are rotated in
x = -0.41, 0.70, 0.58 !bond direction
c = 0.0000, 0.0000, -3.3337:
```

```
dz2 !a1g orbital along z axis
c = 0.0000, 0.0000,-3.3337:
dyz;dxz !e'g orbitals, initial projection
```

The initial projection for e_g states ($d_{3z^2-r^2}$ and $d_{x^2-y^2}$) in VI_3 are set using the local coordinate z' and x' as in CrI_3. The projection for a_{1g} state is set as $d_{3z^2-r^2}$ orbital using the global xyz Cartesian coordinate. Since it is not easy to set the linear combination of orbital states for e'_g state (see. Eq.4.1), the initial projection for e'_g states were set as d_{xz} and d_{yz} orbital states by way of trial. The tight-binding band structures of VI_3 performed with Wannier projections on V-d and I-p orbitals are shown in Fig. 4.3. Our projections were well chosen to represent the orbital states in this work. The unitary transformation and maximally localization process successfully generated the e'_g-like orbital states that show the clear CEF splitting in the projected DOS shown in Fig. 4.4 (b).

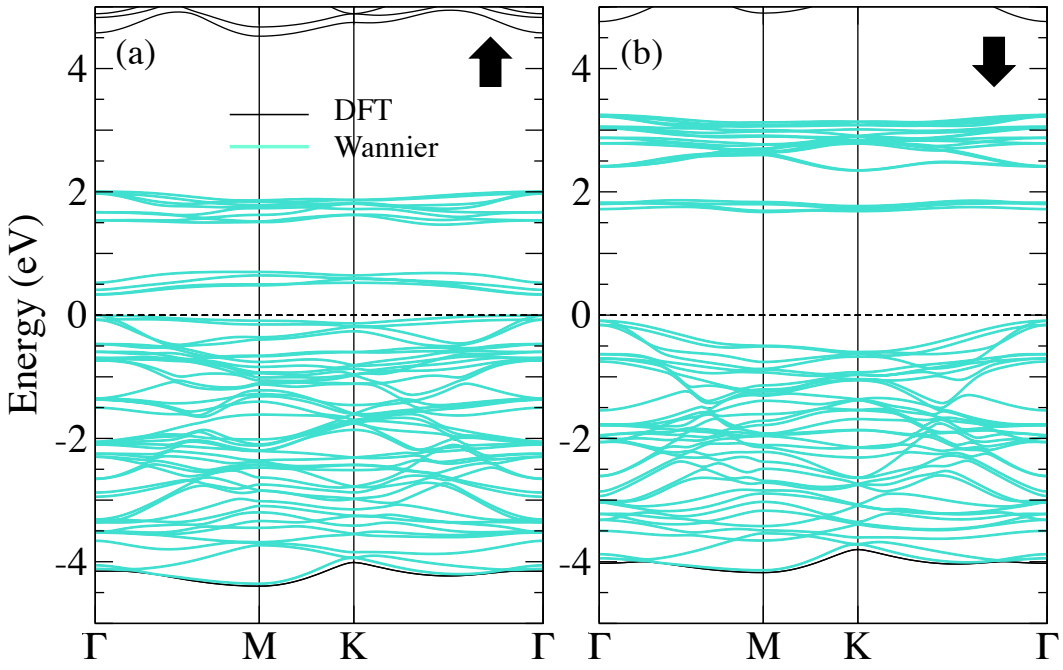

Fig. 4.3 Tight-binding band structures with MLWFs projected to V-d and I$-p$ orbitals for (a) up- and (b) down-spin states. The black curves represent DFT-calculated bands; cyan curves represent tight-binding bands.

After the maximally localization process, the Wannier functions converged to localized orbitals as shown in Fig. 4.2 (e) and (f): orbitals shapes are in accordance with the e_g-t_{2g} states induced by the cubic CEF in CrI_3, and the e_g-(a_{1g}, e'_g) states splitting induced by the trigonal CEF in VI_3. In particular, for the latter, it is possible to recognize the $\left|3z^2 - r^2\right\rangle$

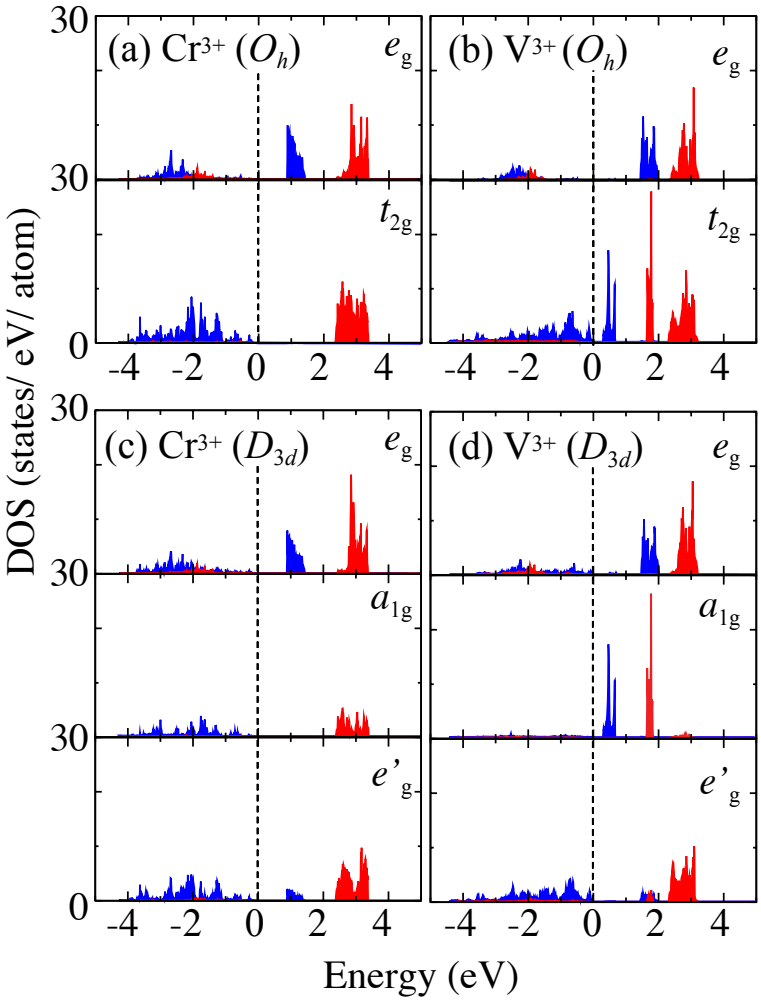

Fig. 4.4 The partial DOS projected onto (a-b) Cr-3*d* and (c-d) V-3*d* with O_h and D_{3d} CEF states, respectively, via Wannier function. Blue (red) color represents for majority spin (minority spin). Fermi level is set at energy origin.

orbital shape for the a_{1g} state, which occupies the empty space at the center of the I_3 triangle and points along the z-direction, and mixed shapes from the ($\left|x^2-y^2\right\rangle, |zx\rangle$) and ($|xy\rangle, |yz\rangle$) orbitals for the e'_{g1} and e'_{g2} states respectively, according to Eq. 4.1.

It is noted that the Cr d^3 partial DOS, projected on the trigonal D_{3d} basic set (Fig. 4.4 (c)), so as to allow a direct comparison with the V d^2 case, shows an overlap in the energy range of the a_{1g} and e'_g, reflecting the absence of splitting induced by the trigonal CEF, in line with the O_h local octahedral symmetry of CrI_3. The partial DOS resolved for each MLWF state for monolayer CrI_3 and VI_3 are shown in Fig. 4.4 (a) and (d), clearly showing the O_h and D_{3d} CEF splitting for CrI_3 and VI_3 respectively, therefore validating our basis functions choice for the Wannier projection. In particular, Cr-d orbital states are split into occupied t_{2g} and empty e_g with a gap of about 0.9 eV in the majority spin channel (up-spin states); the minority spin channel (down-spin states), unoccupied for both orbital types, does not display any relevant splitting. Such a different behavior between the majority and minority spin channels can be ascribed to the *pd* hybridization : the up-spin d-states strongly hybridize with I-p states located at the top of the valence band, causing the large CEF splitting; the down-spin d-states are higher in energy, *i.e.* away from I-p levels, thus not showing any significant CEF splitting. In VI_3, the spin-up channel of the V d states are clearly split into e_g, a_{1g}, e'_g trigonal CEF states. In particular, the e'_g is the lowest energy state with a broad distribution due to the *pd* hybridization below the Fermi level, similar to CrI_3. On the other hand, the CEF splitting shows a different behaviour of the empty d states: the a_{1g} states become the lowest energy states, while the e'_g state still lies in the same energy region as minority Cr-t_{2g} state. This is related to the fact that e'_g state has more bonding character with surrounding I p state than a_{1g} state (compare the orbital shapes in Fig. 4.2(f)); therefore, the *pd* hybridization shifts unoccupied e'_g level up and shifts occupied I-p level down.

4.4.3 Electronic properties of monolayer VI_3

Our DFT calculations converged into two different electronic states, corresponding to half-metallic state [72] and Mott-insulator state [71, 73] as reported in the literature. Two electrons occupy t_{2g} states as $a^1_{1g}e'^1_g$ and $e'^2_g a^0_{1g}$, respectively. Each state can be stabilized according to the initial electronic state that one can set through the density matrix in GGA+U scheme [83]. I confirmed that the insulating state shows the band gap of 0.39 eV/f.u (the value strongly depends on U value) and total energy lower than the half-metallic state by 1.8 eV/f.u.. Hereinafter, I focus on the Mott insulator state as the ground state. Fig. 4.5 show the calculated band structure and total DOS of monolayer VI_3. The conduction band bottom consists of V 3d state, located in an energy range from 0.4 eV $< E - E_F <$ 3.2 eV above the Fermi level. The valence band top consists of I-5p state, strongly hybridize with the occupied

V-3d orbitals. In VI_3 monolayer, the energy difference between intra-layer antiferromagnetic (AFM) and ferromagnetic (FM) were calculated as $\Delta E = E_{\mathrm{AFM}} - E_{\mathrm{FM}} = 12.8$ meV/f.u. manifesting that the FM state is robust. The local magnetic moment was calculated as $S = 2.16\mu_{\mathrm{B}}$.

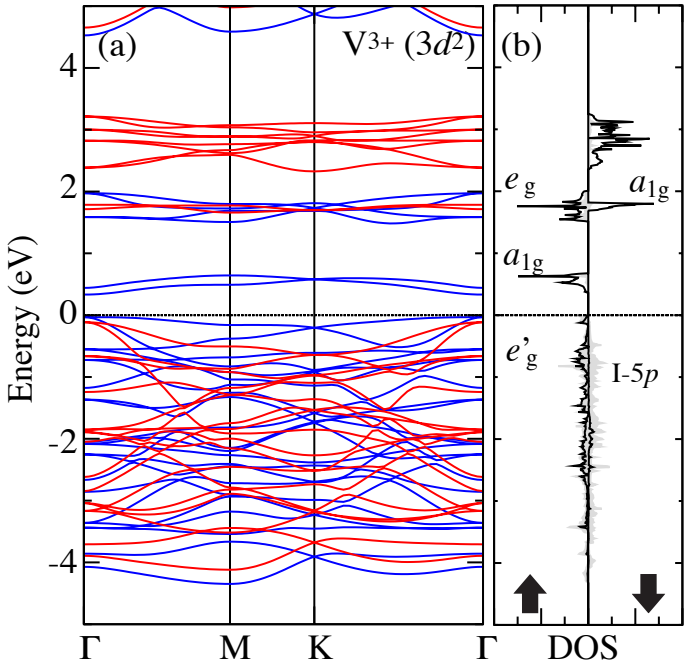

Fig. 4.5 (a) Band structure of monolayer VI_3: blue curve for majority spin and red curve for minority spin. (b) Partial density projected into V-d (black curve) and I-p (grey solid) states. The Fermi energy E_{F} is set at origin of energy.

4.5 Results for bilayer VI_3

4.5.1 Electronic structure of bilayer VI_3

Since the electronic structure doesn't significantly depend on the layer stacking, hereinafter I focus on electronic properties in AB stacking. The calculated band structure and DOS for bilayer VI_3 AB stacking in FM order are shown in Fig. 4.6. The conduction band bottom consists of V-3d state, while the valence band top consists of I-5p state, by which I classify the system as charge-transfer insulator. The occupied V-3d states located in an energy range of -4 eV $< E - E_{\mathrm{F}} < 0$ strongly hybridize with the I-5p orbitals. The energy gap is caluclated as 0.34 eV with the U value of 2 eV.

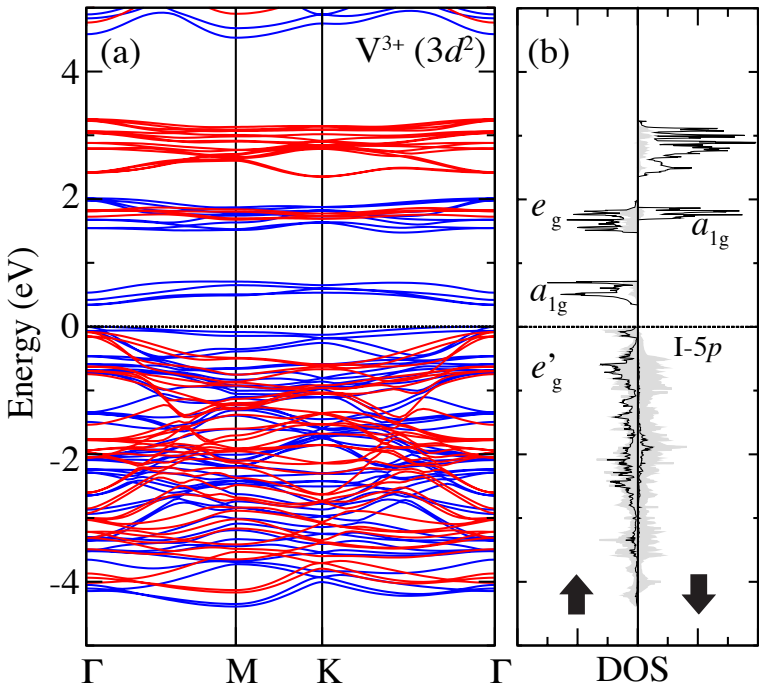

Fig. 4.6 (a) Band structure of bilayer VI_3 in AB stacking pattern: blue curve for majority spin and red curve for minority spin. (b) Partial density projected into V-*d* (black curve) and I-*p* (grey solid) states. The Fermi energy E_F is set at origin of energy.

In Fig. 4.7, I plot the total energy of AB stacking against the interlayer separation with PBE and PBE-D2 approaches. The binding energy is defined as the difference between the minimum value of the total energy in the bilayer and the doubled total energy in the monolayer. The interlayer separation, d, is defined as the out-of-layer-projected distance between inter-layer V neighbors. In the case of using PBE functional, the binding energy is negligible (≈ -0.01 eV/f.u.), manifesting the absence of the explicit dispersion interaction in DFT. Indeed, the use of vdW correction is needed for evaluating the accurate binding energy of layered system such as graphite. The binding energy found at the minimum of the curve with PBE-D2 functional is -0.69 eV/f.u (-0.64 eV/f.u) at the equilibrium separation of 6.665 Å (6.662 Å) in AB (AB') stacking VI_3 bilayer.

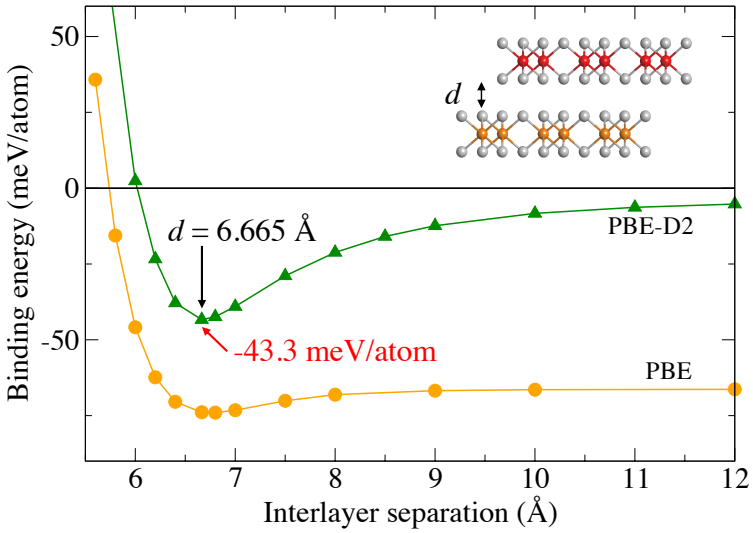

Fig. 4.7 Binding energy calculated as a function of inter-layer distance for bilayer VI_3 AB stacking with PBE (orange curve) and PBE-D2 (green curve) functional.

Although Yang *et.al* proposed that the insulating ground state is stabilized by the spin-orbit coupling (SOC) splitting instead of Mott-Hubbard splitting in monolayer VI_3 [73], here I take it granted that the CEF splitting is more dominant than the SOC splitting as normally seen in 3*d* transition-metal oxides. Nevertheless, I have tested the effect of SOC; in fact, SOC affects the band width and band energy for I-*p* states but it does not significantly change the V 3*d* band structure and does not change our conclusion in this study. With SOC, the gap is close, because I-*p* bands are split and become wider but V-*d* keeps their shapes, as shown in Fig. 4.8 (b). It leads to the shift-down of the conduction band. If I tune U value to U=3.5 eV (Fig. 4.8 (c)) I get the same band structure as what I got in U = 2 eV without SOC (Fig. 4.8 (a)).

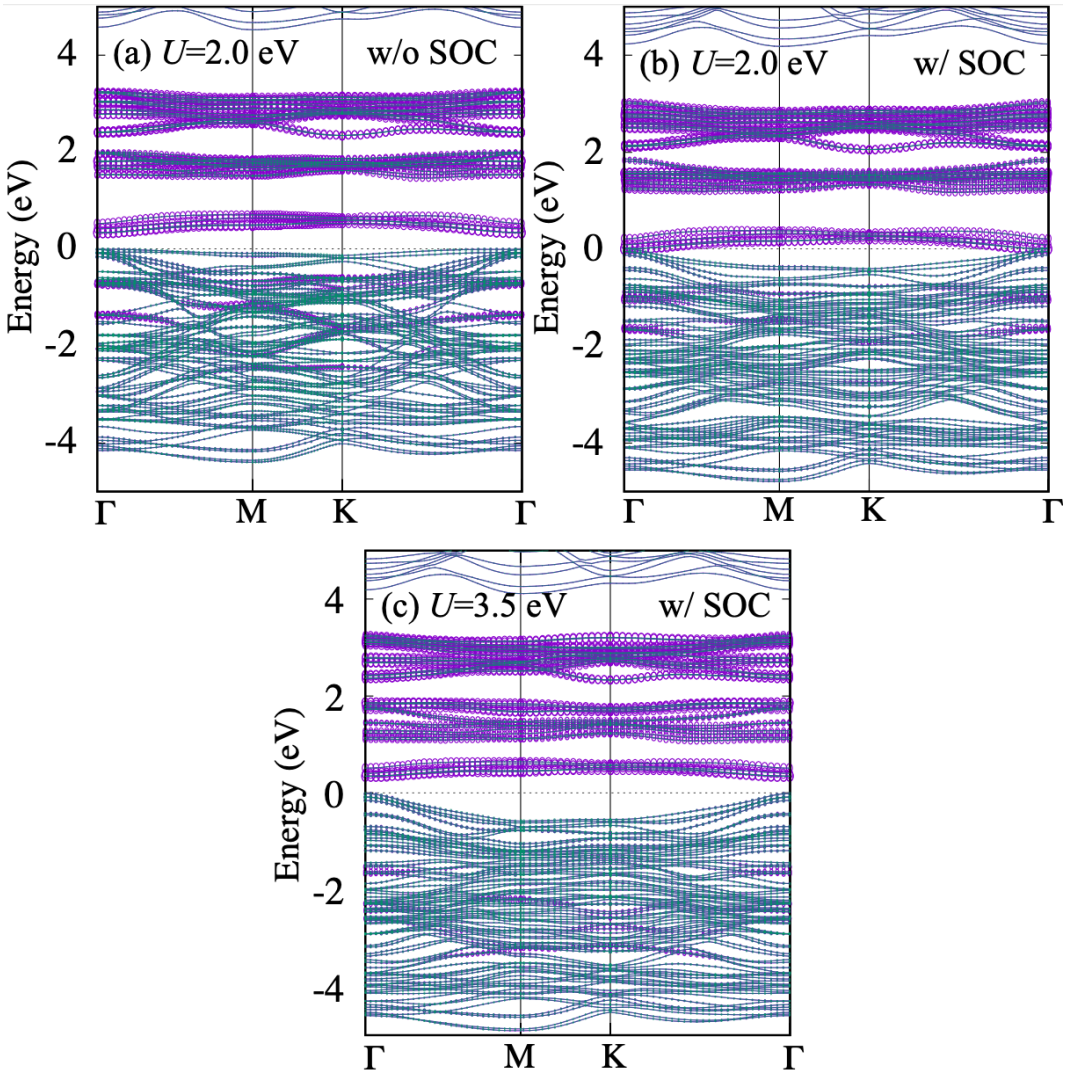

Fig. 4.8 Projected band structures of bilayer VI_3 in AB stacking with $U = 2.0eV$ (a) without SOC, (b) with SOC and (c) $U = 3.5eV$ with SOC. The dark-violet (green) bands stand for the V-d (I-p) bands.

Table 4.1 Relative total energy (meV/f.u) for inter-layer FM and AFM spin configurations in bilayer CrI_3 and VI_3 in AB and AB′ stacking. Lower energy is highlighted.

		AB	AB′
CrI_3	FM	**0**	**34.8**
	AFM	14.7	36.6
VI_3	FM	**0**	2.44
	AFM	0.69	**2.40**

4.5.2 Inter-layer magnetic stability

I calculated the total energy between inter-layer FM and AFM orders for the two stacking in bilayer VI_3 and compared the results with those obtained in CrI_3. In bilayer VI_3, inter-layer FM and AFM spins ordering are very close in energy; nevertheless, the FM order is favored in the AB-stacking, while the AFM order is favored in AB′ stacking, as reported in Table 4.1. Differently, in bilayer CrI_3, FM order is favored in both AB and AB' stacking pattern. Noteworthy, the inter-layer FM order in AB′ stacking is only slightly more stable than the AFM order, the energy differences being rather sensitive to used on-site Coulomb U values, therefore not allowing a direct comparison with previous works on bilayer CrI_3. In any case, according to the energy differences reported in Table 4.1, the magnetic stability in bilayers VI_3 and in CrI_3 AB′-stacking result to be weak. This may lead to an easy control of the magnetism by external electric field or electrostatic doping.

To understand the magnetic stability, the magnetic exchange interactions between V atoms are evaluated by fitting the Heisenberg Hamiltonian to our total energy calculated in AB and AB′ stacking. Here I assume the Heisenberg Hamiltonian,

$$H = \sum_{\langle i,j \rangle} J_{ij} \mathbf{s}_i \cdot \mathbf{s}_j, \tag{4.2}$$

where J_{ij} are the isotropic Heisenberg coupling constant between spins site i and j (parallel spin configuration is favored when $J < 0$ and anti-parallel spin is favored when $J > 0$) and s_i is the unit vector pointing to the direction of the spin at site i.

In addition to the intra-layer (in-plane) first nearest-neighbor coupling ($J_{\parallel}$), I thus considered inter-layer couplings (J_1 and J_2 in AB stacking; J'_1, J'_2, J'_3 and J'_4 in AB′ stacking) as schematically illustrated in Fig. 4.1 (e) and (f); associated atomic pairs distances are reported in Table 4.2. In particular, I performed calculations to estimate J'_2, J'_3 and J'_4 in a $2\times1\times1$ supercell via the four-state energy mapping method [84–88]. This method allows to consider

Table 4.2 Number of equivalent bonds per unit cell N, bond distance between transion-metal sites d, and calculated exchange coupling constants J_{ij} in AB and AB$'$ stacking for bilayer CrI_3 and VI_3.

		AB stacking			AB$'$ stacking				
		$J_{\parallel}$	J_1	J_2	$J'_{\parallel}$	J'_1	J'_2	J'_3	J'_4
CrI_3	N	6	1	9	6	2	2	2	2
	d (Å)	3.95	6.57	7.68	3.95	7.00	7.02	8.03	8.92
	J_{ij} (meV)	-7.03	-0.82	-0.69	-8.11	-0.18	-0.23	-0.29	0.25
VI_3	N	6	1	9	6	2	2	2	2
	d (Å)	3.95	6.66	7.74	3.95	7.04	7.05	8.07	8.95
	J_{ij} (meV)	-3.2	0.81	-0.24	-4.46	0.10	0.21	0.04	-0.04

one specific pair of spins and remove the background interactions, therefore allowing the calculation of the inter-layer magnetic exchange coupling constants of interest.

In Table 4.2 I report the estimated exchange coupling constants for bilayer VI_3 and CrI_3. For CrI_3, the intra-layer and inter-layer exchange coupling overall favor parallel spin states in both AB stacking and AB$'$ stacking. For VI_3, the intra-layer exchange coupling favors parallel spin state, while the inter-layer coupling eventually favors parallel spin state in AB-stacking and anti-parallel spin states in AB'-stacking, (cfr Table 4.1). In closer detail, in AB stacking, J_1 favours anti-parallel coupling (0.81 meV), while J_2 favours parallel coupling (-0.24 meV). Since there is one J_1 bond and nine J_2 bonds per unit cell, the ferromagnetic configuration is more stable. In AB$'$ stacking, both J'_1 and J'_2 favour anti-parallel coupling (0.1 meV and 0.21 meV), thus dominantly contributing to the inter-layer AFM coupling stability.

4.5.3 Virtual hopping mechanism

To understand the microscopic mechanism of the stacking-dependent magnetic couplings, I recall *"virtual hopping"* idea based on the Hubbard model [82]. In the weak hopping limit, the inter-site hopping can be treated as a perturbation to the ground state in which magnetic ordering does not affect the energy. When the hopping process is allowed between occupied and unoccupied states, it in turn contributes to the ground state energy through the second-order contribution as the effective exchange energy $J_{\text{eff}} = 2t^2/U$ with hopping integral t and Coulomb repulsion U, as the process is called virtual hopping. If I consider the direct hopping between occupied and unoccupied $3d$ states at the transition metal sites, parallel-spin configuration is favored if the hopping ($t_{\uparrow\uparrow}$) is strong between majority- and

majority-spin states whereas anti-parallel-spin configuration is favored if the hopping ($t_{\uparrow\downarrow}$) is strong between majority- and minority-spin states. Fig. 4.9 shows the schematic picture of the virtual hopping which describes parallel-spin ($t_{\uparrow\uparrow}$) and anti-parallel-spin ($t_{\uparrow\downarrow}$) hopping in bilayer CrI_3 and VI_3 via CEF splitting.

In order to discuss the virtual hopping process, I extracted the hopping parameters by using MLWF basis set as illustrated in Fig. 4.2 (e) and (f). Note that the WFs are centered at V and Cr sites and spreading the tail to iodine site, so that our virtual hopping process implicitly includes the *pd* hybridization process. The same concept can be found in Anderson's original work on super-exchange interaction [19].

Table 4.3 Hopping integrals calculated by MLWF basis set between occupied and unoccupied *d* orbital states in parallel- ($t_{\uparrow\uparrow}$) or anti-parallel ($t_{\uparrow\downarrow}$) spin configurations. Three types of hopping integrals, t_1, t_2, and t_1', corresponding with inter-layer exchange couplings J_1, J_2, and J_1' are listed. $E_{\uparrow\uparrow}$ ($E_{\uparrow\downarrow}$) (eV) is difference between two eigenenergy for the MLWFs in parallel (anti-parallel) spin configuration. The dominant hopping values relevant to the exchange couplings and those illustrated in Fig. 4.10 (a) and (b) are highlighted by black and red colors, respectively.

CrI_3	Hopping $t_{\uparrow\uparrow}$			Hopping $t_{\uparrow\downarrow}$		
	e_g^0-e_g^0	t_{2g}^3-e_g^0	t_{2g}^3-t_{2g}^3	e_g^0-e_g^0	t_{2g}^3-e_g^0	t_{2g}^3-t_{2g}^0
$E_{\uparrow\uparrow}$ ($E_{\uparrow\downarrow}$)(eV)	0	1.5	0	2.7	4.3	4.6
t_1 (meV)	0.9	**0.6**	0.7	1.3	-1.1	1.7
t_2 (meV)	0.6	**1.5**	0.8	0.6	2.7	-1.3
t_1' (meV)	2.1	**1.3**	1.4	3.0	-3.1	4.6

VI_3	Hopping $t_{\uparrow\uparrow}$				Hopping $t_{\uparrow\downarrow}$				
	$a_{1g}{}^0$-$a_{1g}{}^0$	$e_g{}^0$-$e_g{}^0$	$e_g'{}^2$-$a_{1g}{}^0$	$e_g'{}^2$-$e_g{}^0$	$a_{1g}{}^0$-$a_{1g}{}^0$	$e_g{}^0$-$e_g{}^0$	$e_g'{}^2$-$a_{1g}{}^0$	$e_g'{}^2$-$e_g{}^0$	$e_g'{}^2$-$e_g'{}^0$
$E_{\uparrow\uparrow}$ ($E_{\uparrow\downarrow}$)(eV)	0	0	1.4	1.5	1.4	2.1	2.9	3.4	3.5
t_1 (meV)	-3.6	2.1	**0.0**	-0.7	-4.6	2.7	0.0	1.0	0.6
t_2 (meV)	-0.7	1.1	0.3	**-1.6**	-0.5	-0.9	-0.6	2.6	-1.0
t_1' (meV)	3.6	1.0	-1.1	1.6	4.9	1.1	**-3.1**	3.1	-3.3

Fig. 4.10 shows the inter-layer hopping paths with the corresponding MLWFs which are responsible for the exchange energy in bilayer CrI_3 and VI_3. Here I pick up three typical types of inter-layer exchange couplings: First neighbor and second neighbor (J_1 and J_2) interactions in AB stacking; first neighbor (J_1') interaction in AB' stacking. The calculated hopping integrals are shown in Table 4.3. In AB-stacking bilayer CrI_3, the negative (parallel-spin-favored) J_1 can be explained by a sizable hopping between occupied $d_{zx}\uparrow$ state and unoccupied $d_{x^2-y^2}\uparrow$ state ($t = 0.6$meV). That is basically consistent with the previous works discussing the e_g-t_{2g} hopping [64, 89]. As shown in a figure, the diagonally elongated lobes

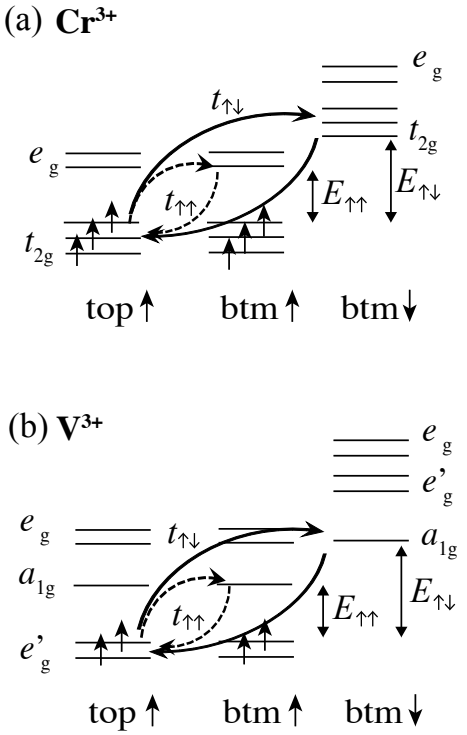

Fig. 4.9 The schematic picture of the virtual hopping in (a) bilayer CrI_3 and (b) bilayer VI_3. Hopping $t_{\uparrow\uparrow}$ refers FM state and hopping $t_{\uparrow\downarrow}$ refers AFM state. $E_{\uparrow\uparrow}$ is the splitting energy from the valence band maximum to the conduction band minimum of the up-spin states. $E_{\uparrow\downarrow}$ is the splitting energy from the valence band maximum of the up-spin states to the conduction band minimum of the down-spin states.

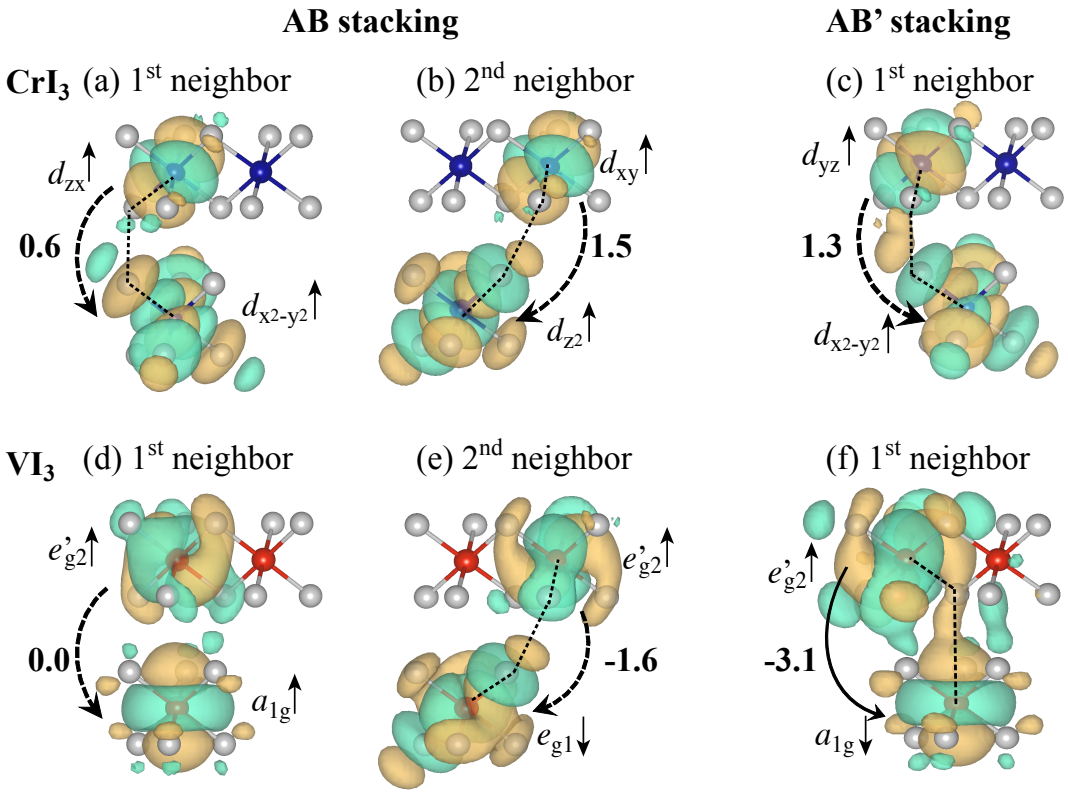

Fig. 4.10 MLWFs relevant to inter-layer exchange coupling in (a-c) bilayer CrI_3 and (d-f) VI_3. ↑ and ↓ denote the majority and minority spin state, respectively. The arrows show the electron hopping from an occupied orbital state to an unoccupied orbital state; the dashed and solid lines denote the parallel-spin and anti-parallel-spin configurations, respectively. Values of the hopping integrals (meV) are also shown nearby the arrows. Isosurface level was set 0.3 for (a-c) and 0.45 for (d-f).

of d_{zx} and $d_{x^2-y^2}$ orbitals makes a path through Cr-I-I-Cr sites with d_{zx}-$p(\pi)$—p-$d_{x^2-y^2}(\sigma)$ hybridization.

In AB-stacking bilayer VI_3, in contrast, the trigonal CEF levels and the two-electron occupation make J_1 positive (anti-parallel-spin-favored). The hopping between $e'_{g2}\uparrow$ and $a_{1g}\uparrow$ states are calculated to be negligible ($t = 0.0$ meV) so that it does not contribute to the magnetic interaction. On the other hand, hopping between $e'_{g2}\uparrow$ and $e_g\downarrow$ states is sizable (t=1.0 meV) which may be responsible for the anti-parallel-spin-favored exchange interaction.

The second neighbor interaction J_2 is negative both for CrI_3 and VI_3. This can be explained by large hopping integral between $d_{xy}\uparrow$ and $d_{z^2}\uparrow$ and that between $e'_{g2}\uparrow$ and $e_{g1}\uparrow$ states. In a figure, one can recognize d_{xy}—p-$d_{z^2}(\sigma)$ hybridization. Same goes for VI_3 case where d_{xy} orbital is just replaced by e'_{g2} orbital.

AB'-stacking bilayer CrI_3 shows similar result to the AB-stacking case; d_{yz}-$p(\pi)$—p-$d_{x^2-y^2}(\sigma)$ hybridization makes J'_1 negative. As making a keen contrast, AB'-stacking bilayer VI_3 shows an interesting aspect of the orbital hybridization. Since a vanadium atom at the lower layer is located right under an iodine atom at the upper layer, V-a_{1g} orbital strongly overlaps I-p_z orbital. This makes the $e'_{g2}\uparrow$-$p(\sigma)$—$a_{1g}\downarrow$ hopping very strong ($t = -3.1$meV) and makes J'_1 positive. In AB' stacking bilayers, the inter-layer exchange interactions are weaker than those in AB stacking bilayers since several possible hoppings between multiple orbital states tends to cancel each other due to the geometry.

4.6 Electric field control of magnetic stability

Finally, I discuss the effect of electric field on the magnetic stability in bilayer VI_3. In Fig. 4.11 the sawtooth-like potential for the application of the external electric field 0.2V/Å is plotted along the z direction, i.e., perpendicular to the slab. The slope of the dashed line relating the four minima at the bottom corresponds to an electric field affecting the slab, which is small compared to the slope in the vacuum region.

The energy difference between inter-layer AFM and FM states in AB and AB' stacking with applied electric fields is shown in Fig. 4.12. In both stacking cases, the electric fields application promotes the FM ordering. Remarkably, in AB′ stacking, it switches the ground state from AFM to FM ordering with the electric fields around 0.1V/Å.

The microscopic mechanism of the tunable magnetic stability can be explained by invoking again the virtual hopping idea. The DOS projected onto V-d orbital state of top and bottom layer in AB′ stacking bilayer VI_3 is shown in Fig. 4.13. Without electric field, DOS of top and bottom layer lie in the same energy range. As discussed above, there is a

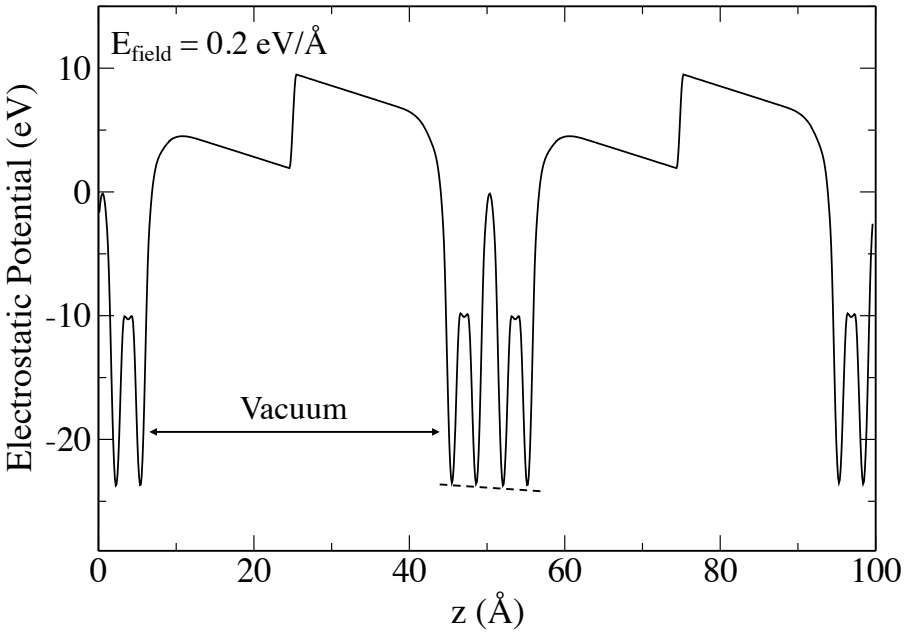

Fig. 4.11 Electrostatic potential plotted along the out-of-plane direction of VI_3 slab with electric field 0.2 V/Å. The in-plane components are averaged. Fermi energy is set as origin of energy. The I atoms are located at four bottoms of valleys, showing the potential slope caused by applied electric field (see the dotted line) The dipole correction is visible as a potential jump in the middle of the vacuum region.

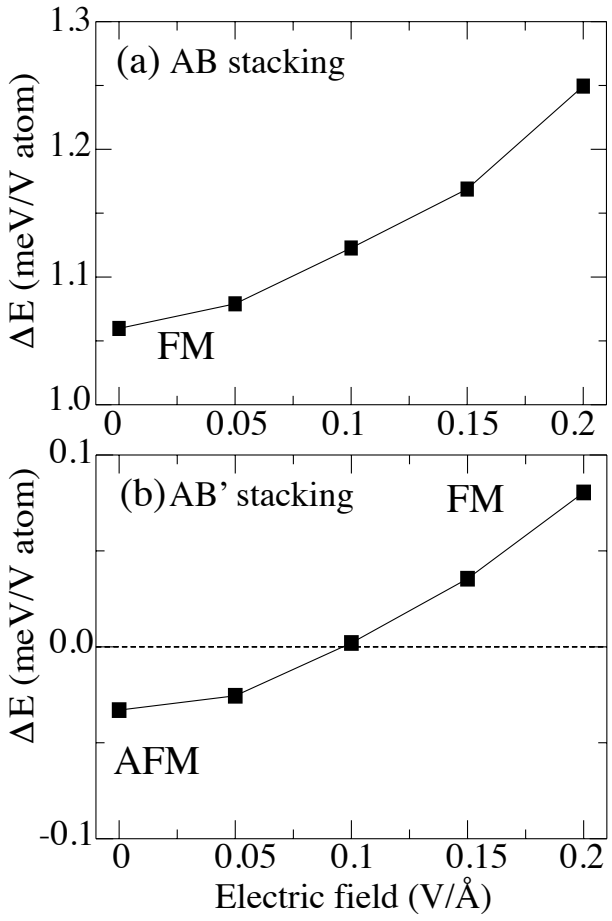

Fig. 4.12 The energy difference between the FM and AFM ordering for (a) AB and (b) AB′ stacking as a function of an external electric field. The positive value of ΔE means FM is favored and negative means AMF is favored.

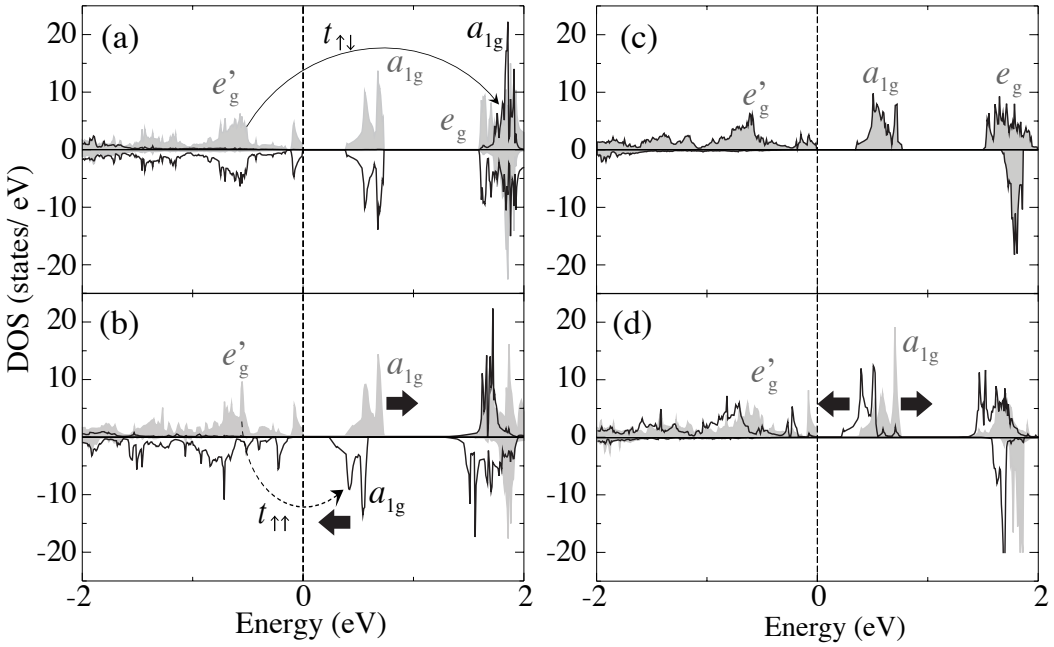

Fig. 4.13 *d*-orbitals projected DOS for top (solid filled) and bottom (solid line) layer of bilayer VI_3 without and with external electric field AB′ stacking in (a)(b) AFM ordering and (c)(d) FM ordering, respectively. Black arrow presents for the energy shifted by applied electric field. $t_{\uparrow\uparrow}$ ($t_{\uparrow\downarrow}$) represents parallel-spin (anti-parallel-spin) hopping. Vertical dash line denote the Fermi energy.

competition between parallel-spin hopping and anti-parallel-spin hopping to determine the first-neighbor exchange coupling J_1'. Since the energy difference between $e_g'^2 \uparrow$ and $a_{1g} \downarrow$ state ($E_{\uparrow\downarrow}$=2.9 eV) is much larger than the energy difference between $e_g' \uparrow$ and $a_{1g} \uparrow$ state ($E_{\uparrow\uparrow}$=1.4 eV), one may think that it stabilizes parallel-spin configuration. However, J_1' is found to be slightly AFM-favored because the anti-parallel spin hopping ($t_{\uparrow\downarrow} = -3.1$ meV) is stronger than the parallel-spin hopping ($t_{\uparrow\uparrow} = -1.1$ meV). With electric fields, the a_{1g} orbital state of top layer is shifted up and bottom layer is shifted down as shown in Fig. 4.13. The band gap becomes narrower due to the shift of DOS and in turn decreases the difference of orbital energy levels, i.e. a denominator of the effective exchange energy $J_{\text{eff}} = 2t_{\uparrow\uparrow}^2/E_{\uparrow\uparrow}$ while the hopping integral is not significantly affected by the electric field. This increases the tendency toward FM stability and switch the magnetic ordering from AFM to FM.

Chapter 5

Summary

First, I systematically investigated the MAE of the Co-based transition-metal thin films by means of first-principles DFT calculations. The results show that the large perpendicular MAE can be achieved by tuning atomic-layer stacking in Ni-Co thin film both in the hcp-like and fcc-like stackings as making a stark contrast to the pure Co thin film that shows perpendicular magnetocrystalline anisotropy only with the hcp stacking. The MAE is decomposed into single-layer contributions and inter-layer contributions to reveal the fact that not only the on-site SOC of 3*d* elements but also the strong hybridization between these elements play an important role to determine the MAE. The small effect of electric fields on the magnetocrystalline anisotropy also has been found in Ni-Co thin film. According to our finding, Ni-Co thin film has the potential for future spintronics applications that may be confirmed by subsequent experimental studies.

Second, first-principles calculations were performed to investigate the magnetic stability in bilayer VI_3 making a comparison with CrI_3. In the trigonal crystal field, the t_2g orbital state are split into a_{1g} and e'_g states. The a_{1g} orbital state has the typical lobe shape pointing to the out-of-plane direction and plays an important role in inter-layer magnetic exchange interaction. The exchange interaction was analyzed by evaluating the hopping integrals between MLWFs projected onto V-*d* orbital states. In AB' stacking bilayer VI_3, the first neighbor inter-layer exchange interaction is determined by the strong hopping between a_{1g} and e'_g states. Since the hopping that favors parallel-spin configuration and that favors anti-parallel-spin configuration are competing, the application of electric field enables to switch the magnetic ordering from inter-layer AFM to FM. This finding may pave the way to the spintronics application of the vdW 2D magnets.

References

[1] S. Methfessel, IEEE Transactions on Magnetics **1**, 144 (1965).

[2] E. Ascher, H. Rieder, H. Schmid, and H. Stössel, Journal of Applied Physics **37**, 1404 (1966).

[3] S. Kanai, M. Yamanouchi, S. Ikeda, Y. Nakatani, F. Matsukura, and H. Ohno, Applied Physics Letters **101**, 122403 (2012).

[4] S. Kanai, Y. Nakatani, M. Yamanouchi, S. Ikeda, H. Sato, F. Matsukura, and H. Ohno, Applied Physics Letters **104**, 212406 (2014).

[5] P. Hohenberg and W. Kohn, Phys. Rev. **136**, B864 (1964).

[6] W. Kohn and L. J. Sham, Phys. Rev. **140**, A1133 (1965).

[7] A. D. Becke, Phys. Rev. A **38**, 3098 (1988).

[8] J. P. Perdew and Y. Wang, Phys. Rev. B **45**, 13244 (1992).

[9] J. P. Perdew, K. Burke, and M. Ernzerhof, Phys. Rev. Lett. **77**, 3865 (1996).

[10] O. Klein, Zeitschrift für Physik **37**, 895 (1926).

[11] W. Gordon, Zeitschrift für Physik **40**, 117 (1926).

[12] P. A. M. Dirac and R. H. Fowler, Proceedings of the Royal Society A: Mathematical, Physical and Engineering Sciences **117**, 610 (1928).

[13] M. Weinert, R. E. Watson, and J. W. Davenport, Phys. Rev. B **32**, 2115 (1985).

[14] J. Neugebauer and M. Scheffler, Phys. Rev. B **46**, 16067 (1992).

[15] L. Bengtsson, Phys. Rev. B **59**, 12301 (1999).

[16] J. Hubbard, Proc. R. Soc. Lond. A **276**, 238 (1963).

[17] G. H. Wannier, Phys. Rev. **52**, 191 (1937).

[18] N. Marzari and D. Vanderbilt, Phys. Rev. B **56**, 12847 (1997).

[19] P. W. Anderson, Phys. Rev. **115**, 2 (1959).

[20] S. Tehrani, J. M. Slaughter, E. Chen, M. Durlam, J. Shi, and M. DeHerren, IEEE Transactions on Magnetics **35**, 2814 (1999).

[21] X. F. Han, Z. C. Wen, and H. X. Wei, Journal of Applied Physics **103**, 07E933 (2008).

[22] K. L. Wang, J. G. Alzate, and P. K. Amiri, Journal of Physics D: Applied Physics **46**, 074003 (2013).

[23] S. Mangin, D. Ravelosona, J. A. Katine, M. J. Carey, B. D. Terris, and E. E. Fullerton, Nature Materials **5**, 210 (2006).

[24] E. Lundgren, B. Stanka, M. Schmid, and P. Varga, Phys. Rev. B **62**, 2843 (2000).

[25] K. Duschek, D. Pohl, S. Fähler, K. Nielsch, and K. Leistner, APL Materials **4**, 032301 (2016).

[26] K. Yakushiji, T. Saruya, H. Kubota, A. Fukushima, T. Nagahama, S. Yuasa, and K. Ando, Applied Physics Letters **97**, 232508 (2010).

[27] J. W. Koo, S. Mitani, T. T. Sasaki, H. Sukegawa, Z. C. Wen, T. Ohkubo, T. Niizeki, K. Inomata, and K. Hono, Applied Physics Letters **103**, 192401 (2013).

[28] S. Ikeda, K. Miura, H. Yamamoto, K. Mizunuma, H. D. Gan, M. Endo, S. Kanai, J. Hayakawa, F. Matsukura, and H. Ohno, Nature Materials **9**, 721 (2010).

[29] P. Bruno, Phys. Rev. B **39**, 865 (1989).

[30] D. Weller, Y. Wu, J. Stöhr, M. G. Samant, B. D. Hermsmeier, and C. Chappert, Phys. Rev. B **49**, 12888 (1994).

[31] D. Weller, J. Stöhr, R. Nakajima, A. Carl, M. G. Samant, C. Chappert, R. Mégy, P. Beauvillain, P. Veillet, and G. A. Held, Phys. Rev. Lett. **75**, 3752 (1995).

[32] J. Stöhr, Journal of Magnetism and Magnetic Materials **200**, 470 (1999).

[33] K. Hotta, K. Nakamura, T. Akiyama, T. Ito, T. Oguchi, and A. J. Freeman, Phys. Rev. Lett. **110**, 267206 (2013).

[34] K. Hayashi, A.-M. Pradipto, K. Nozaki, T. Akiyama, T. Ito, T. Oguchi, and K. Nakamura, Journal of Electronic Materials **48**, 1319 (2019).

[35] C.-G. Duan, J. P. Velev, R. F. Sabirianov, Z. Zhu, J. Chu, S. S. Jaswal, and E. Y. Tsymbal, Phys. Rev. Lett. **101**, 137201 (2008).

[36] M. Tsujikawa and T. Oda, Phys. Rev. Lett. **102**, 247203 (2009).

[37] R. Shimabukuro, K. Nakamura, T. Akiyama, and T. Ito, Physica E: Low-dimensional Systems and Nanostructures **42**, 1014 (2010).

[38] T. Kawabe, K. Yoshikawa, M. Tsujikawa, T. Tsukahara, K. Nawaoka, Y. Kotani, K. Toyoki, M. Goto, M. Suzuki, T. Nakamura, M. Shirai, Y. Suzuki, and S. Miwa, Phys. Rev. B **96**, 220412 (2017).

[39] E. Wimmer, H. Krakauer, M. Weinert, and A. J. Freeman, Phys. Rev. B **24**, 864 (1981).

[40] M. Weinert, E. Wimmer, and A. J. Freeman, Phys. Rev. B **26**, 4571 (1982).

[41] T. Oguchi, in *Interatomic Potential and Structural Stability*, edited by K. Terakura and H. Akai (Springer Berlin Heidelberg, Berlin, Heidelberg, 1993) pp. 33–41.

[42] D. D. Koelling and B. N. Harmon, Journal of Physics C: Solid State Physics **10**, 3107 (1977).

[43] J. M. Soler and A. R. Williams, Phys. Rev. B **42**, 9728 (1990).

[44] G. H. O. Daalderop, P. J. Kelly, and M. F. H. Schuurmans, Phys. Rev. B **41**, 11919 (1990).

[45] X. Wang, D.-S. Wang, R. Wu, and A. J. Freeman, Journal of Magnetism and Magnetic Materials **159**, 337 (1996).

[46] D. Paige, B. Szpunar, and B. Tanner, Journal of Magnetism and Magnetic Materials **44**, 239 (1984).

[47] R. Lizárraga, F. Pan, L. Bergqvist, E. Holmström, Z. Gercsi, and L. Vitos, Scientific Reports **7**, 3778 (2017).

[48] K. Biedermann, M. Gubo, L. Hammer, and K. Heinz, Journal of Physics: Condensed Matter **21**, 185003 (2009).

[49] A. Freeman and R. Wu, Journal of Magnetism and Magnetic Materials **100**, 497 (1991).

[50] G. H. O. Daalderop, P. J. Kelly, and F. J. A. den Broeder, Phys. Rev. Lett. **68**, 682 (1992).

[51] D.-S. Wang, R. Wu, and A. J. Freeman, Phys. Rev. B **47**, 14932 (1993).

[52] M. Mito, H. Ohsumi, T. Shishidou, F. Kuroda, M. Weinert, K. Tsuruta, Y. Kotani, T. Nakamura, Y. Togawa, J. Kishine, Y. Kousaka, J. Akimitsu, and K. Inoue, Phys. Rev. B **99**, 174439 (2019).

[53] T. Burkert, O. Eriksson, S. I. Simak, A. V. Ruban, B. Sanyal, L. Nordström, and J. M. Wills, Phys. Rev. B **71**, 134411 (2005).

[54] C. Andersson, B. Sanyal, O. Eriksson, L. Nordström, O. Karis, D. Arvanitis, T. Konishi, E. Holub-Krappe, and J. H. Dunn, Phys. Rev. Lett. **99**, 177207 (2007).

[55] K. Nakamura, R. Shimabukuro, Y. Fujiwara, T. Akiyama, T. Ito, and A. J. Freeman, Phys. Rev. Lett. **102**, 187201 (2009).

[56] B. Huang, G. Clark, E. Navarro-Moratalla, D. R. Klein, R. Cheng, K. L. Seyler, D. Zhong, E. Schmidgall, M. A. McGuire, D. H. Cobden, W. Yao, D. Xiao, P. Jarillo-Herrero, and X. Xu, Nature **546**, 270 (2017).

[57] C. Gong, L. Li, Z. Li, H. Ji, A. Stern, Y. Xia, T. Cao, W. Bao, C. Wang, Y. Wang, Z. Q. Qiu, R. J. Cava, S. G. Louie, J. Xia, and X. Zhang, Nature **546**, 265 (2017).

[58] Y. Deng, Y. Yu, Y. Song, J. Zhang, N. Z. Wang, Z. Sun, Y. Yi, Y. Z. Wu, S. Wu, J. Zhu, J. Wang, X. H. Chen, and Y. Zhang, Nature **563**, 94 (2018).

[59] B. Huang, G. Clark, D. R. Klein, D. MacNeill, E. Navarro-Moratalla, K. L. Seyler, N. Wilson, M. A. McGuire, D. H. Cobden, D. Xiao, W. Yao, P. Jarillo-Herrero, and X. Xu, Nature Nanotechnology **13**, 544 (2018).

[60] S. Jiang, J. Shan, and K. F. Mak, Nature Materials **17**, 406 (2018).

[61] E. S. Morell, A. León, R. H. Miwa, and P. Vargas, 2D Materials **6**, 025020 (2019).

[62] S. Jiang, L. Li, Z. Wang, K. F. Mak, and J. Shan, Nature Nanotechnology **13**, 549 (2018).

[63] M. A. McGuire, H. Dixit, V. R. Cooper, and B. C. Sales, *Chemistry of Materials*, Chemistry of Materials **27**, 612 (2015).

[64] N. Sivadas, S. Okamoto, X. Xu, C. J. Fennie, and D. Xiao, *Nano Letters*, Nano Letters **18**, 7658 (2018).

[65] D. Soriano, C. Cardoso, and J. Fernández-Rossier, Solid State Communications **299**, 113662 (2019).

[66] P. Jiang, C. Wang, D. Chen, Z. Zhong, Z. Yuan, Z.-Y. Lu, and W. Ji, Phys. Rev. B **99**, 144401 (2019).

[67] J. Kim, K.-W. Kim, B. Kim, C.-J. Kang, D. Shin, S.-H. Lee, B.-C. Min, and N. Park, *Nano Letters*, Nano Letters **20**, 929 (2020).

[68] D.-H. Kim, K. Kim, K.-T. Ko, J. Seo, J. S. Kim, T.-H. Jang, Y. Kim, J.-Y. Kim, S.-W. Cheong, and J.-H. Park, Phys. Rev. Lett. **122**, 207201 (2019).

[69] S. Son, M. J. Coak, N. Lee, J. Kim, T. Y. Kim, H. Hamidov, H. Cho, C. Liu, D. M. Jarvis, P. A. C. Brown, J. H. Kim, C.-H. Park, D. I. Khomskii, S. S. Saxena, and J.-G. Park, Phys. Rev. B **99**, 041402 (2019).

[70] S. Tian, J.-F. Zhang, C. Li, T. Ying, S. Li, X. Zhang, K. Liu, and H. Lei, *Journal of the American Chemical Society*, Journal of the American Chemical Society **141**, 5326 (2019).

[71] Y.-P. Wang and M.-Q. Long, Phys. Rev. B **101**, 024411 (2020).

[72] C. Huang, F. Wu, S. Yu, P. Jena, and E. Kan, Physical Chemistry Chemical Physics **22**, 512 (2020).

[73] K. Yang, F. Fan, H. Wang, D. I. Khomskii, and H. Wu, Phys. Rev. B **101**, 100402 (2020).

[74] J. He, S. Ma, P. Lyu, and P. Nachtigall, J. Mater. Chem. C **4**, 2518 (2016).

[75] T. Kong, K. Stolze, E. I. Timmons, J. Tao, D. Ni, S. Guo, Z. Yang, R. Prozorov, and R. J. Cava, Advanced Materials **31**, 1808074 (2019).

[76] J. A. Wilson, C. Maule, P. Strange, and J. N. Tothill, Journal of Physics C: Solid State Physics **20**, 4159 (1987).

[77] C. Long, T. Wang, H. Jin, H. Wang, and Y. Dai, *The Journal of Physical Chemistry Letters*, The Journal of Physical Chemistry Letters **11**, 2158 (2020).

[78] G. Kresse and J. Furthmüller, Phys. Rev. B **54**, 11169 (1996).

[79] S. L. Dudarev, G. A. Botton, S. Y. Savrasov, C. J. Humphreys, and A. P. Sutton, Phys. Rev. B **57**, 1505 (1998).

[80] A. A. Mostofi, J. R. Yates, Y.-S. Lee, I. Souza, D. Vanderbilt, and N. Marzari, Computer Physics Communications **178**, 685 (2008).

[81] W. B. Wu, D. J. Huang, J. Okamoto, A. Tanaka, H.-J. Lin, F. C. Chou, A. Fujimori, and C. T. Chen, Phys. Rev. Lett. **94**, 146402 (2005).

[82] D. I. Khomskii, *Transition Metal Compounds* (Cambridge University Press, 2014).

[83] A. I. Liechtenstein, V. I. Anisimov, and J. Zaanen, Phys. Rev. B **52**, R5467 (1995).

[84] H. J. Xiang, E. J. Kan, S.-H. Wei, M.-H. Whangbo, and X. G. Gong, Phys. Rev. B **84**, 224429 (2011).

[85] H. Xiang, C. Lee, H.-J. Koo, X. Gong, and M.-H. Whangbo, Dalton Trans. **42**, 823 (2013).

[86] D. Šabani, C. Bacaksiz, and M. V. Milošević, Phys. Rev. B **102**, 014457 (2020).

[87] C. Xu, J. Feng, S. Prokhorenko, Y. Nahas, H. Xiang, and L. Bellaiche, Phys. Rev. B **101**, 060404 (2020).

[88] X. Changsong, F. Junsheng, X. Hongjun, and B. Laurent, npj Comput. Mater.) **4**, 57 (2018).

[89] S. W. Jang, M. Y. Jeong, H. Yoon, S. Ryee, and M. J. Han, Phys. Rev. Materials **3**, 031001 (2019).

Appendix A

Technique for relativistic spin-polarized calculation

A technique for relativistic spin-polarized calculations was described by Koelling and Harmon (1977) [42]. The technique for reduction of the Dirac equation, which initially neglects the spin-orbit interaction to keep spin as a good quantum number, and retains all other relativistic kinematic effects such as mass-velocity, Darwin term, and higher order terms is included. The spin-orbit coupling, furthermore, can be included as a perturbation after the scalar relativistic spin-polarized wave functions have been obtained.

Although more general potentials can be easily adopted, here we assume that the relativistic interaction only inside the muffin-tin spheres, the solution of the Dirac equation with the central-force potential is of the form

$$\Psi_{\kappa\zeta} = \begin{bmatrix} g_\kappa \chi_{\kappa\zeta} \\ -i f_\kappa \sigma_r \chi_{\kappa\zeta} \end{bmatrix} \tag{A.1}$$

where the radial functions g_κ and f_κ satisfy the following radial equation:

$$g'_\kappa = -\frac{(\kappa+1)}{r} g_\kappa + 2Mc f_\kappa \tag{A.2}$$

$$f'_\kappa = \frac{1}{c}(V-E) g_\kappa + \left(\frac{\kappa-1}{r}\right) f_\kappa \tag{A.3}$$

with the relativistic mass

$$M \equiv m + \frac{1}{2c^2}(E-V) \tag{A.4}$$

In which, Eqs. A.2 and A.3 show the differentiation with respect to the radius r of g_κ and f_κ; κ is the usual relativistic quantum number giving both l and j; anf $\chi_{\kappa\zeta}$ is the two-component spinor which is the relativistic equivalent of the spherical harmonics. The energy E is defined with the rest mass as $E = mc^2$. By solving the Eq. A.2 for f_κ and substitute it into Eq. A.3 we obtain

$$\frac{-1}{2M}\left[g''_\kappa + \frac{2}{r}g'_\kappa - \frac{l(l+1)}{r^2}g_\kappa\right] - \frac{V'g'_\kappa}{4M^2c^2} + Vg_\kappa - \frac{\kappa+1}{r}\frac{V'g_\kappa}{4M^2c^2} = Eg_\kappa. \tag{A.5}$$

In the above equation, only last term depends on the sign of κ, which is called the spin-orbit term. It gives us a difficulty in solving the Eq. A.5 since spin is no more a good quantum number. To solve Eq. A.5, the spin-orbit interaction is dropped and the a weighted sum of the orbital at the muffin-tin radius is used to obtain logarithmic derivatives. For more suitable approach, let's define a new function ϕ_κ by

$$\phi_\kappa \equiv \frac{1}{2Mc}g'_\kappa \tag{A.6}$$

which is related by Eq. A.2 to f_κ

$$f_\kappa = \phi_\kappa + \frac{1}{Mcr}(\kappa+1)g_\kappa \tag{A.7}$$

Combining Eq. A.6 together with Eq. A.7, dropping the last term, we get

$$\phi'_l = -\frac{2}{r}\phi_l + \left[\frac{l(l+1)}{2Mcr^2} + \frac{1}{c}(V-E)\right]g_l \tag{A.8}$$

where the κ index has been replaced by l since there is no longer any j dependence. Now, Eq. A.6 and A.8 are a coupled set of liner equations and can be solved as,

$$\phi_{\kappa\zeta} \simeq \begin{bmatrix} g_l\chi_{\kappa\zeta} \\ -i\left[\phi_l + \frac{(\kappa+1)}{2Mcr}g_l\right]\sigma_r\chi_{\kappa\zeta} \end{bmatrix} \tag{A.9}$$

Now we can combine functions $\kappa = l$ and $\kappa = -(l+1)$ with the appropriate Clebsch-Gordan coefficients to bring a function back to the familiar non-relativistic quantum numbers (lms) as,

$$\phi_{lms} = \begin{bmatrix} g_l Y_{lm}\chi_s \\ \frac{i}{2Mc}\sigma_t\left(-g'_l + \frac{1}{r}g_l\sigma\cdot\mathbf{L}\right)Y_{lm}\chi_s \end{bmatrix} \tag{A.10}$$

where χ_s is the usual up (down) spinor. We see that still there are some mixture of spin in the small component. A simple solution is to neglect the small component since g_l contains the desired relativistic corrections. After we obtain Eq. A.10, the spin-orbit interaction term can be included to the full Hamiltonian by second variational method.

Appendix B

Second variation procedure

As we discuss in section 2.2.3 that the full relativistic Hamiltonian can be simplified to

$$(H_{\text{scalar}} + H_{\text{SOC}})\Psi_n^{\mathbf{k}}(\mathbf{r}) = \varepsilon_n^{\mathbf{k}}(\mathbf{r})\Psi_n^{\mathbf{k}}(\mathbf{r})(\mathbf{r}), \tag{B.1}$$

After solving the scalar relativistic equation in A, now we treat the spin-orbit term by introducing a perturbed wave function expanded by the non-perturbed wavefunctions,

$$\Psi_n^{\mathbf{k}}(\mathbf{r}) = \sum_{i,\sigma} c_{ni\sigma}^{\mathbf{k}} \Psi_{0i\sigma}^{\mathbf{k}}(\mathbf{r}) \tag{B.2}$$

where n are perturbed band index, i are non-perturbed index and σ are spin index.

After solving the secular equation:

$$\langle \psi_i^{\mathbf{k},\sigma} | H_{\text{SO}} | \psi_i'^{\mathbf{k},\sigma'} \rangle = \varepsilon_i^{\mathbf{k}} \psi_i^{\mathbf{k},\sigma}, \tag{B.3}$$

eigenenergy $\varepsilon_n^{\mathbf{k}}$ and eigenfunction $c_{ni\sigma}$ are obtained. It should be noted that this procedure break the degeneracy of the spin-degenerate bands and the new wavefunction $\Psi_n^{\mathbf{k}}(\mathbf{r})$ will be described as a mixed state of both up-spin and down-spin states. The spin density functional which can be expressed as

$$n_\sigma(\mathbf{r}) = \sum_{n,\mathbf{k}} \left(\sum_i c_{in\sigma}^{\mathbf{k}} \Psi_{0i\sigma}^{\mathbf{k}}(\mathbf{r}) \right)^2 \tag{B.4}$$

must be calculated separately.

Including H_{SOC} term in the relativistic calculation, the variational treatment is more precise than a one-time perturbation calculation. In the first order of perturbation, the energy shift is almost zero since the SOC term vanishes for unperturbed states. In the second-order of

perturbation, however, the energy difference induced by the SOC comes from the interaction between the occupied and unoccupied states is presented as

$$\begin{aligned} E_{\mathrm{SOC}} &= \sum_{o,u} \frac{|\langle o|H_{\mathrm{SOC}}|u\rangle|^2}{\varepsilon_u - \varepsilon_o} \\ &= \xi \sum_{o,u} \frac{|\langle o|\mathbf{S}\cdot\mathbf{L}|u\rangle|^2}{\varepsilon_u - \varepsilon_o}. \end{aligned} \tag{B.5}$$

List of Publications

Papers

1. T. P. T. Nguyen, K. Yamauchi, K. Nakamura, and T. Oguchi, *"Impact of Inter-site Spin–Orbit Coupling on Perpendicular Magnetocrystalline Anisotropy in Cobalt-Based Thin Films"*, Journal of the Physical Society of Japan, **89**, 114710 (2020).

2. T. P. T. Nguyen, K. Yamauchi, D. Amoroso, S. Picozzi, and T. Oguchi, *"Magnetic properties of bilayer VI_3: Role of trigonal crystal field and electric-field tuning"*, submitted to Physical Review B.

Oral Presentations

1. T. P. T. Nguyen, K. Nakamura, and T. Oguchi, *"Perpendicular magnetocrystalline anisotropy by tuning atomic-layer alignment in 3d transition-metal thin films"*, The Physical Society of Japan Annual Meeting, Osaka, March 2017.

2. T. P. T. Nguyen, K. Yamauchi, and T. Oguchi, *"Perpendicular Magnetocrystalline Anisotropy on 3d Transition-Metals Multilayers – A First-principles Study"*, American Physical Society March Meeting, Boston, USA, March 2019.

3. T. P. T. Nguyen, K. Yamauchi, and T. Oguchi, *"Control of magnetism in bilayer VI_3 by an external electric field"*, FMS-NANOMATA, Da Nang, Vietnam, November 2019.

4. T. P. T. Nguyen, K. Yamauchi, and T. Oguchi, *"Electric-Field Control of 2D Magnetism in Bilayer VI_3"*, The Spin-RNJ Young Researcher Online Workshop, June 2020.

Poster Presentations

1. T. P. T. Nguyen, K. Nakamura, and T. Oguchi, *"Perpendicular magnetocrystalline anisotropy of 3d transition-metal thin films"*, The 19^{th} Asian Workshop on First-Principles Electronic Structure Calculations, Hsinchu, Taiwan, October 2016.

2. T. P. T. Nguyen, K. Nakamura, and T. Oguchi, *"Perpendicular magnetocrystalline anisotropy in 3d transition-metal thin films for spintronic devices"* SpinTECH IX International School and Conference, Fukuoka, Japan, June 2017.

3. T. P. T. Nguyen, K. Nakamura, and T. Oguchi, *"Tuning Atomic-Layer Alignment for Perpendicular Magnetocrystalline Anisotropy of Co/Ni Multilayers"*, The 5^{th} International Conference of Asian Union of Magnetics Societies (IcAUMS 2018), Jeju, Korea, June 2018.

4. T. P. T. Nguyen, K. Nakamura, and T. Oguchi, *"First-principles Study of Perpendicular Magnetocrystalline Anisotropy on Co/Ni Multilayers"*, International Conference on Magnetism (ICM 2018), San Francisco, USA, July 2018.

5. T. P. T. Nguyen, K. Nakamura, and T. Oguchi, *"First-principles calculation of the magnetocrystalline anisotropy of Co-based thin films"*, The Physcical Society of Japan Autumn Meeting, Kanazawa, September 2016.

6. T. P. T. Nguyen, K. Nakamura, and T. Oguchi, *"Perpendicular magnetocrystalline anisotropy in Co-based 3d transition-metal thin films by first-principles study"*, Junjirou Kanamori Memorial International Symposium, Tokyo, September 2017.

7. T. P. T. Nguyen, K. Nakamura, and T. Oguchi, *"Mechanism of perpendicular magnetocrystalline anisotropy in 3d transition-metal thin films by first-principles study"*, JIM Autumn Meeting, Sapporo, September 2017.

8. T. P. T. Nguyen, *"First-principles Study on Electric Field Control of Magnetism in Bilayer VI3"*, The 22^{nd} Asian Workshop on First-Principles Electronic Structure Calculations, Osaka, Japan, October 2019.

9. T. P. T. Nguyen, K. Yamauchi, K. Nakamura, and T. Oguchi, *"Electric Field Effect on Magnetocrystalline Anisotropy in 3d Transition-metal Thin Films"*, Materials Research Meeting, Yokohama, Japan, December 2019.

10. T. P. T. Nguyen, K. Yamauchi, and T. Oguchi, *"Role of trigonal crystal field in the magnetic property in bilayer VI_3"*, The 25^{th} symposium on the Physics and Applications of Spin-related Phenomena in Semiconductors, online November 2020.